

1 **10–year satellite–constrained fluxes of ammonia improve**
2 **performance of chemistry transport models**

3

4 **Nikolaos Evangeliou^{1,*}, Yves Balkanski², Sabine Eckhardt¹, Anne Cozic², Martin**
5 **Van Damme³, Pierre-François Coheur³, Lieven Clarisse³, Mark W. Shephard⁴,**
6 **Karen E. Cady-Pereira⁵, Didier Hauglustaine²**

7

8 ¹Norwegian Institute for Air Research (NILU), Department of Atmospheric and Climate
9 Research (ATMOS), Kjeller, Norway.

10 ²Laboratoire des Sciences du Climat et de l'Environnement (LSCE), CEA-CNRS-UVSQ,
11 91191, Gif-sur-Yvette, France.

12 ³Université libre de Bruxelles (ULB), Spectroscopy, Quantum Chemistry and Atmospheric
13 Remote Sensing (SQUARES), Brussels, Belgium.

14 ⁴Environment and Climate Change Canada, Toronto, Ontario M3H 5T4, Canada.

15 ⁵Atmospheric and Environmental Research, Inc., Lexington, MA, USA.

16

17 * Corresponding author: N. Evangeliou (Nikolaos.Evangeliou@nilu.no)

18

19 **Abstract**

20 In recent years, ammonia emissions have been continuously increasing being almost four
21 times higher than in the 20th century. Although an important species as its use as a fertilized
22 sustains human living, ammonia has major consequences both for humans and the environment,
23 because of its reactive gas phase chemistry that makes it easily convertible to particles. Despite
24 its pronounced importance, yet, ammonia emissions are highly uncertain in most emission
25 inventories. However, the great development of satellite remote sensing nowadays provides the
26 opportunity for more targeting research in constraining ammonia emissions. Here, we used
27 satellite measurements to calculate global ammonia emissions over the period 2008–2017.
28 Then, the calculated ammonia emissions were fed to a chemistry transport model and ammonia
29 concentrations were simulated for the period 2008–2017.

30 The simulated concentrations of ammonia were compared with ground measurements
31 from Europe, North America and Southeastern Asia, as well as with satellite measurements.
32 The satellite-constrained ammonia emissions represent global concentrations more accurately
33 than state-of-the-art emissions. Calculated fluxes in the North China Plain were seen more
34 increased after 2015, not due to emission changes, but due to changes in sulfate emissions that
35 resulted in less ammonia neutralization and hence in larger atmospheric loads. Emissions over
36 Europe were also twice as much as those in traditional datasets with dominant sources to be
37 industrial and agricultural applications. Four hot-spot regions of high ammonia emissions were
38 seen in North America characterized by large agricultural activity, animal breeding, animal
39 farms, and animal breeding and agricultural practices. South America is dominated by ammonia
40 emissions from biomass burning, which cause a strong seasonality. In Southeastern Asia,
41 ammonia emissions from fertilizer plants in China, Pakistan, India and Indonesia are the most
42 important, while a strong seasonality was observed with a spring and late summer peak due to
43 rice and wheat cultivation. Measurements of ammonia surface concentrations were better
44 reproduced with satellite-constrained emissions, so as measurements from CrIS (Cross-track
45 Infrared Sounder).

Deleted: , which underestimate ammonia with a factor of two

Deleted: (Colorado)

Deleted: (Iowa, northern Texas and Kansas)

Deleted: (Salt Lake, Cache, and Utah)

Deleted: (California)

Deleted: Modelled concentrations from the satellite-constrained ammonia emissions are overestimated in Eastern Europe, where state-of-the-art emissions capture observations better. ...

Deleted: in North America

Deleted: while all emissions generally underestimate station concentrations in Southeastern Asia. The calculated ammonia emissions also reproduce global...

Deleted: observations more effectively

Formatted: Font: Font colour: Text 1

61 **1 Introduction**

62 Ammonia (NH₃) has received a lot of attention nowadays due to its major implications
63 for the population and the environment (Erisman, 2004; Erisman et al., 2007). These include
64 eutrophication of semi-natural ecosystems and acidification of soils (Stevens et al., 2010),
65 secondary formation of particulate matter in the atmosphere (Anderson et al., 2003), and
66 alteration of the global greenhouse balance (De Vries et al., 2011). More specifically in the
67 troposphere, ammonia reacts with the abundant sulfuric and nitric acids (Malm, 2004)
68 contributing 30 % to 50 % of the total aerosol mass of PM_{2.5} and PM₁₀ (Anderson et al., 2003).
69 Ammonium aerosols are therefore a very important component in regional and global aerosols
70 processes (Xu and Penner, 2012) also having significant implications for human health (Aneja
71 et al., 2009). Ammonia alters human health indirectly mainly through formation of PM_{2.5} (Gu
72 et al., 2014) that penetrate the human respiratory systems and deposit in the lungs and alveolar
73 regions (Pope III et al., 2002) causing premature mortality (Lelieveld et al., 2015). As regards
74 to the climate impact, the same ammonium aerosol particles affect Earth's radiative balance,
75 both directly by scattering incoming radiation (Henze et al., 2012) and indirectly as cloud
76 condensation nuclei (Abbatt et al., 2006). They may also cause visibility problems and
77 contribute to haze effect due to secondary PM formation.

78 Sources of ammonia include wild animals (Sutton et al., 2000), ammonia-containing
79 watersheds (Sørensen et al., 2003), traffic (Kean et al., 2009), sewage systems (Reche et al.,
80 2012), humans (Sutton et al., 2000), biomass burning (Sutton et al., 2008) and domestic coal
81 combustion (Fowler et al., 2004), volcanic eruptions (Sutton et al., 2008) and agriculture
82 (Erisman et al., 2007). The latter is responsible for the majority of ammonia global atmospheric
83 emissions. Specifically, in the United States and Europe about 80% of all emissions is related
84 to agriculture (Leip et al., 2015). Emissions have increased considerably since pre-industrial
85 times and are unlikely to decrease due to the growing demand for food and feed (Aneja et al.,
86 2008).

87 The growing attention in ammonia levels has enabled many monitoring actions in Europe
88 (European Monitoring and Evaluation Programme, EMEP), in Southeastern Asia (East Asia
89 acid deposition NETwork) and in the North America (Ammonia Monitoring Network in the
90 US, AMoN-US; National Air Pollution Surveillance Program (NAPS) sites in Canada) to
91 record surface concentrations of ammonia continuously. Recently, several satellite products
92 have been also developed in an effort to identify global levels of ammonia considering that the

93 relatively sparse existing monitoring network has an insufficient coverage for this purpose.
94 These are derived from satellite sounders as the Infrared Atmospheric Sounding Interferometer
95 (IASI) (Van Damme et al., 2017), the Atmospheric Infrared Sounder (AIRS) (Warner et al.,
96 2017), the Cross-track Infrared Sounder (CrIS) (Shephard and Cady-Pereira, 2015), the
97 Tropospheric Emission Spectrometer (TES) (Shephard et al., 2015), and Greenhouse Gases
98 Observing Satellite (Someya et al., 2020). Both IASI and CrIS ammonia products are being
99 continuously compared and evaluated against other observations and products. Relevant
100 analyses include comparison against column-integrated levels measured by Fourier transform
101 infrared spectroscopy (FTIR) (Dammers et al., 2016, 2017), ground-based measurements (Van
102 Damme et al., 2015; Kharol et al., 2018), bottom-up emissions (Van Damme et al., 2018;
103 Dammers et al., 2019) and atmospheric chemistry transport models (CTMs) (Shephard et al.,
104 2020; Whitburn et al., 2016a).

105 Despite its importance, ammonia is a poorly quantified trace gas, with uncertainties over
106 50% on the global emission budget and even higher on temporal and local scales (Dentener and
107 Crutzen, 1994; Faulkner and Shaw, 2008; Reis et al., 2009) and up to 300% for the agricultural
108 sector in Europe (European Environment Agency, 2019). In the present paper, we grid 10 years
109 (2008–2017) of satellite measurements of ammonia retrieved from IASI to calculate monthly
110 surface emissions (hereafter named NE) (see section 2). The same is done using the gridded
111 IASI ammonia column concentrations from Van Damme et al. (2018) (named as VD0.5 and
112 VDgrlf) (see section 2). The three different emission inventories together with a state-of-the-
113 art one, which is more often used by models (named as EGG), are then imported in a CTM to
114 simulate ammonia for the same 10-year period. More details of the different emissions used
115 here are shown in sections [2.4](#), and [2.1](#). Finally, an evaluation of simulated surface
116 concentrations against ground-based measurements from different monitoring stations and
117 satellite products allow to quantify the improvements in ammonia emissions.

118 **2 Methods**

119 **2.1 LMDz-OR-INCA chemistry transport model**

120 The Eulerian global CTM LMDz-OR-INCA was used to calculate ammonia lifetime, as
121 well as to simulate ammonia concentrations from the emission fluxes calculated from IASI
122 satellite products. The model couples the LMDz (Laboratoire de Météorologie Dynamique)
123 General Circulation Model (GCM) (Hourdin et al., 2006) with the INCA (INteraction with
124 Chemistry and Aerosols) model (Folberth et al., 2006; Hauglustaine et al., 2004) and with the

Deleted: 2.3

Deleted: 2.4

127 land surface dynamical vegetation model ORCHIDEE (ORganizing Carbon and Hydrology In
128 Dynamic Ecosystems) (Krinner et al., 2005). In the present configuration, the model has a
129 horizontal resolution of $2.5^{\circ} \times 1.3^{\circ}$, the vertical dimension is divided into 39 hybrid vertical
130 levels extending to the stratosphere. Large-scale advection of tracers is calculated from a
131 monotonic finite-volume second-order scheme (Hourdin and Armengaud, 1999), deep
132 convection is parameterized according to the scheme of Emanuel, (1991), while turbulent
133 mixing in the planetary boundary layer (PBL) is based on a local second-order closure
134 formalism. More information and a detailed evaluation of the GCM can be found in Hourdin et
135 al. (2006).

136 The model simulates atmospheric transport of natural and anthropogenic aerosols
137 recording both the number and the mass of aerosols. The aerosol size distribution is represented
138 using a modal approach that consists of the superposition of 5 log-normal modes that represent
139 both the size spectrum and whether the aerosol is soluble or insoluble (Schulz, 2007). The
140 aerosols are treated in three particle modes, sub-micronic (diameter $< 1 \mu\text{m}$) corresponding to
141 the accumulation mode, micronic (diameter $1\text{--}10 \mu\text{m}$) corresponding to coarse particles, and
142 super-micronic or super coarse particles (diameter $> 10 \mu\text{m}$). LMDz-OR-INCA accounts for
143 emissions, transport (resolved and sub-grid scale), and dry and wet (in-cloud/below-cloud
144 scavenging) deposition of chemical species and aerosols interactively. LMDz-OR-INCA
145 includes a full chemical scheme for the ammonia cycle and nitrate particle formation, as well
146 as a state-of-the-art $\text{CH}_4/\text{NO}_x/\text{CO}/\text{NMHC}/\text{O}_3$ tropospheric photochemistry. Further details
147 about specific reactions, reaction rates and other information entering into the description of
148 the ammonia cycle can be found in Hauglustaine et al. (2014).

149 The global transport of ammonia was simulated from 2007 to 2017 (2007 was the spin-
150 up period) by nudging the winds of the 6-hourly ERA Interim Reanalysis data (Dee et al., 2011)
151 with a relaxation time of 10 days (Hourdin et al., 2006). For the calculation of ammonia's
152 lifetime, the model ran with traditional emissions for anthropogenic, biomass burning and
153 oceanic emission sources using emissions from ECLIPSEv5 (Evaluating the CLimate and Air
154 Quality ImPacts of Short-livEd Pollutants), GFED4 (Global Fire Emission Dataset) and GEIA
155 (Global Emissions InitiAtive) (hereafter called EGG) (Bouwman et al., 1997; Giglio et al.,
156 2013; Klimont et al., 2017).

157 **2.2 Satellite ammonia**

158 **2.2.1 IASI ammonia**

159 The Infrared Atmospheric Sounding Interferometer (IASI) onboard the MetOp-A satellite
160 measures Earth's infrared radiation twice a day in a spectral range of 645–2,760 cm⁻¹ with an
161 elliptical footprint with a diameter of 12 km at nadir (Clerbaux et al., 2009). Due to the larger
162 thermal conditions that lead to smaller uncertainties, only morning data were used in the present
163 assessment (Clarisse et al., 2010). Van Damme et al. (2018) reported limited impact of the IASI
164 overpasses of 4%±8% on ammonia. The 10-year dataset used here is ANNI-NH3-v2.1R-I
165 product (Van Damme et al., 2017) and relies on ERA-Interim ECMWF meteorological input
166 data (Dee et al., 2011). The Artificial Neural Network for IASI (ANNI) algorithm converts the
167 hyperspectral range index to a column-integrated NH₃ value (Whitburn et al., 2016a). The
168 latter relies on the fact that the indices can be converted to a column by taking into account the
169 spectral sensitivity to the ammonia abundance in the observed scene. The hyperspectral range
170 indexes are derived from linear retrievals using a constant gain matrix which includes a
171 generalized error covariance matrix (Van Damme et al., 2014b; Whitburn et al., 2016a). The
172 dataset also provides cloud coverage for each measurement (August et al., 2012). Only
173 measurements with a cloud fraction below 10% were processed in consistency with Van
174 Damme et al. (2018). Cloud coverage was not provided for all measurements until March 2010
175 resulting in smaller data availability before that date. Van Damme et al. (2014a) reported that
176 IASI better measures ammonia in spring and summer months, due to the strong dependence on
177 thermal contrast (error below 50%). For an individual observation, an IASI-retrieved column
178 is considered detectable when the vertical column density exceeds 9.68×10¹⁵ molecules cm⁻²
179 (surface concentration > 1.74 µg m⁻³) at a thermal contrast of 20 K, while the vertical column
180 density should be larger than 1.69×10¹⁶ molecules cm⁻² (3.05 µg m⁻³) at 10 K (Van Damme et
181 al., 2014a). Although the retrieval algorithm uses a fixed vertical profile, extended validation
182 of the resulting dataset has verified small uncertainties (Van Damme et al., 2015, 2018;
183 Dammers et al., 2016; Whitburn et al., 2016b). For instance, Van Damme et al. (2018) reported
184 a difference of 2%±24% (global average) in column-integrated ammonia using different
185 vertical profiles in the retrieval algorithm.

186 **2.2.2 CrIS ammonia**

187 The Cross-Track Infrared Sounder (CrIS) was first launched on the NASA Suomi
188 National Polar-orbiting Partnership (S-NPP) satellite on 28 October 2011 in a sun-synchronous
189 low Earth orbit. The CrIS sensor provides soundings of the atmosphere with a spectral

Field Code Changed

Formatted: Norwegian Bokmål

Formatted: Norwegian Bokmål

190 resolution of 0.625 cm^{-1} (Shephard et al., 2015). One of the main advantages of CrIS is its
191 improved vertical sensitivity of ammonia closer to the surface due to the low spectral noise of
192 $\sim 0.04\text{K}$ at 280K in the NH_3 spectral region (Zavalyov et al., 2013) and the early afternoon
193 overpass that typically coincides with high thermal contrast, which is optimal for thermal
194 infrared sensitivity. The CrIS Fast Physical Retrieval (CFPR) (Shephard and Cady-Pereira,
195 2015) retrieves an ammonia profile (14 levels) using a physics-based optimal estimation
196 retrieval, which also provides the vertical sensitivity (averaging kernels) and an estimate of the
197 retrieval errors (error covariance matrices) for each measurement. As peak sensitivity is
198 typically in the boundary layer between 900 and 700 hPa (~ 1 to 3 km) (Shephard et al., 2020),
199 the surface and total column concentrations are both highly correlated with the retrieved levels
200 in the boundary layer. Shephard et al. (2020) reports estimated total column random
201 measurement errors of 10–15%, with estimated total random errors of $\sim 30\%$. The individual
202 profile retrieval levels have estimated random measurement errors of ~ 10 to 30 %, with
203 estimated total random errors increasing to 60 to 100% due to the limited vertical resolution.
204 These vertical sensitivity and error output parameters are also useful for using CrIS
205 observations in applications (e.g. data fusion, data assimilation; model-based emission
206 inversions (e.g., Cao et al., 2020; Li et al., 2019) as a satellite observational operator can be
207 generated in a robust manner. The detection limit of CrIS measurements has been calculated
208 down to 0.3–0.5 ppbv (Shephard et al., 2020). CrIS ammonia has been evaluated against other
209 observations over North America with the Ammonia Monitoring Network (AMoN) (Kharol et
210 al., 2018) and against ground-based Fourier transform infrared (FTIR) spectroscopy
211 observations (Dammers et al., 2017) showing small differences and high correlations.

212 **2.3 Inverse Distance Weighting (IDW) interpolation**

213 To process large amounts of measurements in a 2-dimensional grid of high resolution,
214 oversampling methods (Streets et al., 2013) can be used (Van Damme et al., 2018). However,
215 considering that the resolution of the CTM is $2.5^\circ \times 1.3^\circ$ (see section 2.4), there is no need to
216 process the measurements on such a high-resolution grid and therefore an interpolation method
217 was used. The method has been extensively used after the Chernobyl accident in 1986 to
218 process more than 500 thousand deposition measurements over Europe (De Cort et al., 1998;
219 Evangeliou et al., 2016).

220 IASI total column ammonia measurements were interpolated onto a grid of $0.5^\circ \times 0.5^\circ$
221 using a modified Inverse Distance Weighting (IDW) algorithm described by (Renka, 1988).

222 This method is preferred due to its ease of use and to its high quality of interpolation. The IDW
223 interpolation is defined by:

$$224 \quad \hat{v}(x, y) = \frac{\sum_{i=1}^n w_i v_i}{\sum_{i=1}^n w_i} \quad \text{Eq. 1}$$

225 where $\hat{v}(x, y)$ is the interpolated value at point (x, y) , w_1, \dots, w_i are the relative weights and
226 v_1, \dots, v_n are the observation values. The weights are defined by the inverse distance functions:

$$227 \quad w_i = \left(\frac{r_w - d_i}{r_w d_i} \right)^2 \quad \text{Eq. 2}$$

$$228 \quad \text{for } (r_w - d_i) = \begin{cases} r_w - d_i & \text{if } d_k < r_w, \\ 0 & \text{if } d_k \geq r_w. \end{cases}$$

229 where r_w denotes the radius of influence of the point (x_i, y_i) , d_i the Euclidean distance
230 between point (x, y) and (x_i, y_i) , and d_k is the threshold distance. We used a threshold
231 distance (d_k) of 50 km, which is similar to the size of each grid cell; different d_k values were
232 included in a sensitivity study (see section 4.2). The Euclidean distance is calculated using
233 Vincenty's formulae (Vincenty, 1975). Finally, the gridded IASI total column ammonia was re-
234 gridding to the model resolution ($2.5^\circ \times 1.3^\circ$) using bilinear interpolation.

Deleted: 4.3

235 2.4 Emission flux calculation of ammonia

236 The emission fluxes of ammonia were calculated using a 1-dimensional box model that
237 assumes first-order loss terms for ammonia and has been already used previously (Van Damme
238 et al., 2018; Whitburn et al., 2016b). It takes into account the gridded column concentrations of
239 ammonia that were calculated with the IDW interpolation method and all the potential removal
240 processes of ammonia occurring in a hypothetical atmospheric box according to the following
241 equation:

$$242 \quad E_{NH_3} = M_{NH_3} / \tau \quad \text{Eq. 3}$$

243 where M_{NH_3} is the mass of ammonia in each atmospheric box (grid-cell) in molecules cm^{-2} and
244 τ is the lifetime of ammonia in the box (given in seconds).

245 Van Damme et al. (2018) assumed a constant lifetime for ammonia, admitting that this is
246 a limiting factor of their study on the basis that chemical loss and deposition are highly variable
247 processes that can change the lifetime drastically. To tackle the large variability of the lifetime
248 of ammonia, we used monthly gridded lifetime calculated from a CTM. This gives robustness
249 in the calculated emissions fluxes considering that at regions where sulfuric and nitric acids are
250 abundant, the chemical loss will be more intensive and, thus, lifetime will be much shorter
251 affecting emissions dramatically.

253 The lifetime (τ) of ammonia in each grid-box results from the three processes affecting
254 ammonia concentrations: transport (t_{trans}) in and out of the grid-cell, chemical loss (t_{chem})
255 and deposition (t_{depo}):

$$256 \quad \frac{1}{\tau} = \frac{1}{t_{trans}} + \frac{1}{t_{chem}} + \frac{1}{t_{depo}} \quad \text{Eq. 4}$$

257 In a CTM, the lifetime can be easily calculated from the species mass balance equation (Croft
258 et al., 2014):

$$259 \quad \frac{dC(t)}{dt} = S(t) - \frac{C(t)}{\tau(t)} \quad \text{Eq. 5}$$

260 where $C(t)$ is the atmospheric burden of ammonia at time t , $S(t)$ is the time-dependent source
261 emission fluxes and $\tau(t)$ is the removal timescale. Assuming steady-state conditions and
262 considering that emission fluxes of ammonia are continuous, there is a quasi-equilibrium
263 between sources and removals of ammonia (Dentener and Crutzen, 1994), and the modeled
264 lifetime of ammonia τ_{mod} can be defined as:

$$265 \quad \tau_{mod} = \frac{C_{NH_3}}{L_{NH_3}^{trans,chem,depo}} \quad \text{Eq. 6}$$

266 where C_{NH_3} is the atmospheric burden of ammonia and $L_{NH_3}^{trans,chem,depo}$ is the total loss due to
267 any process affecting ammonia in the model (transport, chemical reactions, deposition).

268 We calculate ammonia emission fluxes using IASI satellite measurements that we
269 interpolated (see section 2.3) to the model resolution ($2.5^\circ \times 1.3^\circ$) and applying a variable
270 lifetime taken from a CTM (hereafter NE emissions). We also calculate ammonia emissions
271 from the oversampled IASI data of Van Damme et al. (2018), after bilinear re-gridding to the
272 model resolution ($2.5^\circ \times 1.3^\circ$), applying a constant lifetime for ammonia of 12 hours (hereafter
273 VD0.5 emissions) and the same variable lifetime from a CTM as in the NE emissions (hereafter
274 VDgrlf emissions).

275 3 Results

276 In this section, the main results of the monthly emissions (NE) are presented for the 10-
277 year period (2008–2017) of IASI observations. We first describe the monthly modelled
278 ammonia lifetimes (section 3.1). Then, we explain the main characteristics of the obtained
279 emissions (section 3.2) and compare them with those calculated using the IASI gridded
280 products from Van Damme et al. (2018) (VD0.5 and VDgrlf), as well as the ones from the state-
281 of-the-art inventories of EGG and EDGARv4.3.1-GFED4 (Crippa et al., 2016; Giglio et al.,

282 2013) that are often used in CTMs (section 3.3). We finally turn our focus to emissions at
283 continental regions and document their seasonal variation in emissions (section 3.4).

284 **3.1 Modelled lifetime of ammonia**

285 The lifetime of ammonia has been reported to range from a few hours to a few days
286 (Behera et al., 2013; Pinder et al., 2008) so ammonia can only be transported over relatively
287 short distances. This short spread of ammonia is also due to the fact that (a) the majority of its
288 emissions are surface ones (major source is agricultural activity), and (b) its surface deposition
289 velocities are high for most surfaces (Hov et al., 1994). The atmospheric lifetimes of ammonia
290 were summarized in Van Damme et al. (2018). Specifically, Quinn et al. (1990) and more
291 recently Norman and Leck (2005) reported lifetimes of a few hours in the West Pacific, South
292 Atlantic and Indian Oceans, which is in agreement with Flechard and Fowler (1998), who
293 reported a 2-hour lifetime in an area of Scotland where most sources are of agricultural origin.
294 Similar to them, Dammers et al. (2019) recently reported a lifetime estimated from satellite
295 measurements of 2.35 ± 1.16 hours for large point sources based on satellite measurements. The
296 majority of ammonia lifetimes reported regionally or globally fall within 10 and 24 hours
297 independently of the different approaches (Hauglustaine et al., 2014; Hertel et al., 2012; Möller
298 and Schieferdecker, 1985; Sutton et al., 1993; Whitburn et al., 2016b), while Dentener and
299 Crutzen (1994) reported slightly higher lifetimes within a range between 0.9 and 2.1 days
300 depending on ammonia emission fraction of natural origin. Monthly averaged atmospheric
301 ammonia lifetimes in the present study were derived using the version of the LMDz-OR-INCA
302 that includes non-methane hydrocarbons (Hauglustaine et al., 2004).

303 Ammonia lifetime depends on numerous factors such as the presence of ammonia's
304 reactants (sulfuric and nitric acids, through SO_2 and NO_x emissions), meteorological parameters
305 (atmospheric water vapour, and temperature, atmospheric mixing and advection) and ammonia
306 emissions. In ammonia-poor conditions, all ammonia is rapidly removed by neutralising
307 sulfuric acid with an intermediate production of bisulfate. If ammonia increases further
308 (ammonia-rich conditions), then reaction with nitric acid occurs forming nitric ammonium. At
309 this point, the ammonia/sulfuric acid/nitric acid equilibrium becomes very fragile. If sulfate
310 concentrations decrease, then free ammonia is produced, which gradually reacts with nitric acid
311 resulting in production of aerosol phase nitric ammonium. But if particles are aqueous, then
312 sulfate ions in solution increase the equilibrium vapour pressure of ammonia with nitric acid
313 reversing the reaction towards gaseous phase reactants. So, sulfate reductions are linked with

314 non-linear increases of aerosol nitrates and decreases of aerosol ammonium and water (Seinfeld
315 and Pandis, 2000).

316 The calculated ammonia lifetime is shown in **Figure 1a** averaged for the whole study
317 period. The average lifetime was calculated to be 11.6 ± 0.6 hours, which is in the range of the
318 previously reported values. Lower values (~10 hours) were observed in clean remote areas
319 characterized by low ammonia emissions (e.g., Amazon forest, Sahara and Australia), while in
320 the rest of the globe the lifetime was closer to the average value. The highest lifetimes (~16
321 hours) occur over Southern Brazil and Venezuela, which are both areas with relatively high
322 ammonia emissions and low sulfuric and nitric acid concentrations (**Figure 1c**). These
323 conditions are characterized by a low atmospheric sulfuric and nitric acids availability to
324 remove ammonia rapidly, hence causing an increase in lifetime.

325 3.2 Satellite-constrained emissions

326 The average ammonia emissions calculated from the 10-year IASI observations are
327 shown in **Figure 1b** (also in **Figure S 1a**), the reactants' atmospheric burden in **Figure 1c** and
328 their seasonal variability in **Figure 1d** together with monthly modelled lifetimes. The year-by-
329 year total ammonia emissions are depicted in **Figure S 1**, with a monthly temporal resolution.
330 Emissions decline from 242 Tg yr^{-1} in 2008 to 212 Tg yr^{-1} in 2011. In 2012 – 2014, emissions
331 show little variation (194 , 204 and 195 Tg yr^{-1} , respectively), before they increase steeply to
332 248 Tg yr^{-1} in 2015. Finally, in 2016 and 2017 they remain at the same high level (197 and 227
333 Tg yr^{-1} , respectively).

334 The global average annual emission calculated from VD0.5 amounts to 189 Tg (9-year
335 average), which is comparable to the average of the 10-year period that we have calculated in
336 the present study (average \pm sd: $213 \pm 18.1 \text{ Tg yr}^{-1}$). The increase in the emissions we calculate
337 during 2015 and 2017 stand out. The explanation for these increases could be twofold. If sulfur
338 dioxide (a precursor of sulfates) emissions decreased over time, less sulfates are available to
339 neutralize ammonia, hence resulting in higher ammonia column concentrations seen by IASI
340 that could be attributed to new emissions erroneously (see section 2.4). This has been already
341 reported for the North China Plain. To improve air quality, the Chinese government
342 implemented new emission regulations aimed at decreasing the national total NO_x emissions
343 by 10% between 2011 and 2015 (Liu et al., 2017). Several recent studies (Duncan et al., 2016;
344 Krotkov et al., 2016) have highlighted the effectiveness of the air quality policy, as evidenced

Deleted: Figure 1

Deleted: Figure 1

Deleted: Figure 1

Deleted: Figure S 1

Deleted: Figure 1

Deleted: Figure 1

Deleted: Figure S 1

Formatted: Subscript

352 by a decreasing trend in nitrogen dioxide columns over China since 2012. The same has been
353 reported for the sulfur dioxide emissions (Koukouli et al., 2018; Krotkov et al., 2016; Wang et
354 al., 2013). If sulfur dioxide and sulfates presented a constant year-by-year pattern or even
355 increased, then the calculated ammonia emissions would be likely realistic.

Formatted: English (US)

Formatted: English (US)

356 To sort out between these two possibilities, we used sulfur dioxide measurements from
357 NASA's Ozone Monitoring Instrument (OMI, Yang et al., 2007) instrument, whereas sulfate
358 column concentrations were taken from the Modern-Era Retrospective Analysis for Research
359 and Applications, Version 2 (MERRA2, Gelaro et al., 2017) reanalysis data from NASA's
360 Global Modeling and Assimilation Office (GMAO). **Figure S 2** shows timeseries of column
361 concentrations of sulfur dioxide and sulfates from OMI and MERRA2 averaged globally, for
362 continental regions (Europe, North America, South America, Africa), as well as for regions
363 where ammonia emissions are particularly high (India and Southeastern Asia, North China
364 Plain). Although column concentrations of both sulfur dioxide and sulfates present strong
365 interannual variability (**Figure S 2**), their global concentrations show a strong decreasing trend
366 after 2015. **The observed decrease** indicates that sulfate amounts that neutralize ammonia and
367 form ammonium sulfate, thus it is likely that the higher ammonia concentrations seen from
368 IASI after 2015 are not necessarily a result of emission increases. This is not seen from the
369 respective precursor of the atmospheric nitric acid, nitrogen dioxide (**Figure S 2**).

Deleted: Figure S 2

Deleted: Figure S 2

Deleted: T

Deleted: is

Deleted: Figure S 2

370 Looking closely into regions with large changes in ammonias reactants and/or their
371 precursors after 2015 (**Figure 2**), we immediately see that a region of interest is the North China
372 Plain. The North China Plain has been identified as an ammonia hotspot mainly due to extensive
373 agricultural activities (Clarisse et al., 2009; Pan et al., 2018). Liu et al. (2018) reported a sulfur
374 dioxide reduction of about 60% over the recent few years in the North China Plain, sulfates
375 decreased by 50%, while ammonia emissions declined by only 7% due to change in agricultural
376 practices. The suggested decrease in ammonia reactants over the North China Plain is illustrated
377 by the calculated sulfur dioxide column concentration anomaly from OMI (**Figure 2**) and by
378 the sulfate concentration anomaly from MERRA-2 after 2015 (the highest calculated one)
379 (**Figure S 3**). Nitrogen dioxide concentration do not show any noticeable annual change, despite
380 their strong seasonal cycle (**Figure S 2**). The IASI-constrained ammonia emissions calculated
381 here show only a tiny increase of 0.19 ± 0.04 kt y^{-1} after 2015 in the North China Plain and of
382 10 ± 3.1 Tg y^{-1} globally with respect to the 10-year average (**Figure 2**). This is due to the change
383 of sulfur dioxide and nitrogen oxide emission regulations in China, which in turn led to reduced

Formatted: Space After: 10 pt

Deleted: Figure 2

Deleted: Figure 2

Deleted: Figure S 3

Deleted: Figure S 2

Deleted: Figure 2

394 inorganic matter (sulfates, nitrates and ammonium) resulting in regional increases of gaseous
395 ammonia (Lachatre et al., 2019).

396 It should be noted here that decreases in sulfur dioxide and nitrogen dioxide have been
397 reported to have occurred since 2005, at least in Eastern USA and to a lesser extent in Eastern
398 Europe (Krotkov et al., 2016). At the same time, sulfur dioxide and nitrogen dioxide
399 concentrations had started increasing after 2005 in India, a country that shows the largest
400 agricultural activity in the world. The latter has balanced the global sulfur dioxide and nitrogen
401 dioxide budget, explaining that the decreasing trend after 2015 that we report has been affected
402 by our choice to present global averages.

403 3.3 Comparison with traditional emission datasets

404 In this section, we quantify the main differences of our IASI-constrained emission dataset
405 with other state-of-the-art inventories used in global models and for different applications (air
406 quality, climate change etc...). Aside from comparing our emissions with those calculated using
407 Van Damme et al. (2018) data with a constant lifetime (hereafter called VD0.5), we extend our
408 comparison to more traditional datasets such as those of ECLIPSEv5-GFED4-GEIA (EGG) for
409 2008–2017, and EDGARv4.3.1-GFED4 (Crippa et al., 2016; Giglio et al., 2013) for 2008–2012
410 period. Finally, the ammonia emissions presented in this study (NE emissions) are compared
411 to emissions calculated from Van Damme et al. (2018) gridded IASI column data applying a
412 variable (modelled) ammonia lifetime presented in [Figure 1b](#) (hereafter referred as VDgrlf).

413 The 10-year comparison of our calculated emissions with VD0.5 is shown in [Figure 3](#).
414 The 10-year average difference amounts to 29 ± 15 Tg yr⁻¹ (average \pm sd). In all years, the largest
415 differences could be seen over Latin America and over tropical Africa. Our emissions (NE)
416 show a different structure in the Indo-Gangetic Plain and situated slightly more northerly than
417 those in VD0.5. The difference might be due to the IDW interpolation used to process the IASI
418 ammonia in the NE emissions compared with the oversampling method used in VD0.5 (see
419 section 2.3). Nevertheless, Northern India has been identified as a hot-spot region for ammonia,
420 mainly due the importance of agricultural activities in the region (Kuttippurath et al., 2020;
421 Tanvir et al., 2019).

422 [Figure S 4](#) and [Figure S 5](#) present a comparison of our calculated emissions (NE) with
423 the basic state-of-the-art datasets of EGG and EDGARv4.3.1-GFED4, respectively. In both
424 datasets, ammonia emissions remain almost constant over time (average \pm sd: 65 ± 2.8 Tg yr⁻¹

Field Code Changed

Deleted: Figure 1

Deleted: Figure 3

Deleted: Figure S 4

Deleted: Figure S 5

429 and $103 \pm 5.5 \text{ Tg yr}^{-1}$, respectively). The total calculated ammonia emissions in EGG and
430 EDGARv4.3.1-GFED4 are up to three times lower than those calculated from NE (average \pm sd:
431 $213 \pm 18.1 \text{ Tg yr}^{-1}$) or from VD0.5 (9-year average: 189 Tg yr^{-1}). This results in 10-year annual
432 differences that are very significant (average \pm sd: $150 \pm 19.3 \text{ Tg yr}^{-1}$ and $111 \pm 19.2 \text{ Tg yr}^{-1}$,
433 respectively); the largest differences appear over South America (EGG: $7.1 \pm 0.3 \text{ Tg yr}^{-1}$, VD0.5:
434 22 Tg yr^{-1} , NE: $28 \pm 3.0 \text{ Tg yr}^{-1}$, VDgrlf: $24 \pm 1.3 \text{ Tg yr}^{-1}$), while European emissions are
435 practically identical in all datasets except EGG (EGG: $6.9 \pm 1.1 \text{ Tg yr}^{-1}$, VD0.5: 11 Tg yr^{-1} , NE:
436 $15 \pm 2.2 \text{ Tg yr}^{-1}$, VDgrlf: $11 \pm 1.0 \text{ Tg yr}^{-1}$). Emissions from South China Plain are much higher in
437 the two traditional datasets than those presented in this paper (EGG: $25 \pm 1.2 \text{ Tg yr}^{-1}$, VD0.5: 36
438 Tg yr^{-1} , NE: $38 \pm 2.8 \text{ Tg yr}^{-1}$, VDgrlf: $39 \pm 1.8 \text{ Tg yr}^{-1}$). Ammonia emissions derived over China
439 in this work (NE) are among the highest worldwide ([Figure S 1](#)), which agrees well with the 9-
440 year average emissions calculated in VD0.5 inventory over China (see [Figure 3](#)). To assess to
441 which extent emissions from EGG and EDGARv4.3.1-GFED4 are underestimated can only be
442 done by comparing ammonia with ground or satellite observations.

443 The comparison of the annual ammonia emissions in the NE dataset to the modified
444 VDgrlf emissions is shown in [Figure S 6](#). The latter showed a better agreement to the emissions
445 presented in this study with mean annual different of $14 \pm 19 \text{ Tg yr}^{-1}$ (average \pm sd). Previously
446 observed emission differences in the two state-of-the-art inventories over South America and
447 Africa have been now minimized, as well as the displacement north of the Indo-Gangetic Plain
448 emissions remains important. Nevertheless, the smaller differences of our emissions (NE) from
449 those of VDgrlf as compared with the respective difference from the VD0.5 emissions, show
450 the large impact that a more realistic variable lifetime might have in emission calculations with
451 this methodology in these regions.

452 3.4 Site-specific ammonia emissions and seasonal variation

453 [Figure 4](#) illustrates specific regions that show the largest ammonia emissions (Europe,
454 North America, South America and Southeastern Asia). These emissions correspond to the
455 IASI-constrained emissions calculated in this study (NE) and are presented as total annual
456 emissions averaged over the 10-year period of study. At the bottom panels of the same figure,
457 the seasonal variation of the emissions is shown for each of the four hot-spot regions and each
458 of the 10 years of the study.

Deleted: Figure S 1

Deleted: Figure 3

Deleted: Figure S 6

Formatted: Font: Bold

Deleted: Figure 4

463 European total ammonia emissions were estimated to be $15 \pm 2.2 \text{ Tg yr}^{-1}$ (average \pm sd),
464 more than double compared with those reported in EGG ($6.9 \pm 1.1 \text{ Tg yr}^{-1}$) and similar to those
465 in VD0.5 (11 Tg yr^{-1}) or those in VDgrlf ($11 \pm 1.0 \text{ Tg yr}^{-1}$). The greatest emissions were
466 calculated for Belgium, the Netherlands and the Po Valley in Italy (Figure 4). High emissions
467 are also found in North and Northwestern Germany and over Denmark. In contrast, very low
468 emissions are found in Norway, Sweden and parts of the Alps. It is not possible to quantitatively
469 distinguish between different sources of ammonia. It has been reported that approximately 75%
470 of ammonia emissions in Europe originate from livestock production (Webb et al., 2005), and
471 90% from agriculture in general (Leip et al., 2015). More specifically, ammonia is emitted from
472 all stages of manure management, from livestock buildings during manure storage and
473 application to land, as well as from livestock urine. These emissions are strong over most of
474 Northwestern European countries, although sources like fertilization and non-agricultural
475 activities (traffic and urban emissions) can be also important. An example is Tange in Germany,
476 which shows a late summer peak due to growing crops application. No obvious seasonality in
477 the emissions can be seen for Europe as a whole, as the hot-spot regions are rather few compared
478 to the overall surface of Europe. An exception to this stable emission situation over the year
479 occurs during 2010 and during 2015, years for which a late summer peak. In 2010, large
480 wildfires in Russia resulted in high ammonia emissions (R'Honi et al., 2013), while year 2015
481 has been also characterized as an intense fire year (though not like 2010), with fires occurring
482 in Eurasia (Min Hao et al., 2016).

Deleted: Figure 4

483 North America and in particular the US (Figure 4) has been characterized by four hot-
484 spot regions. First, a small region in Colorado, Central US, which is the location of a large
485 agricultural region that traditionally releases large ammonia emissions (Malm et al., 2013).
486 Another example is the state of Iowa (home to more than 20 million swine, 54 million chickens,
487 and 4 million cattle), northern Texas and Kansas (beef cattle), and southern Idaho (dairy cattle)
488 (McQuilling, 2016). Furthermore, the three major valleys in Salt Lake, in Cache, and in Utah
489 in the midwestern US show an evident, but lower intensity hot-spot, as they are occupied by
490 massive pig farms associated to open waste pits. The largest emissions were calculated for the
491 San Joaquin Valley in California (vegetables, dairy, beef cattle and chickens) and further to the
492 South (Tulare and Bakersfield), an area characterized by feedlots (Van Damme et al., 2018;
493 McQuilling, 2016). North American annual ammonia emissions over the 10-year period were
494 averaged $1.1 \pm 0.1 \text{ Tg yr}^{-1}$ (average \pm sd). These values are over two orders of magnitude higher
495 than those in EGG ($0.062 \pm 0.0013 \text{ Tg yr}^{-1}$). Note that his estimate is three times lower than those

Deleted: Figure 4

498 reported in VD0.5 (3.1 Tg yr^{-1}) or in VDgrlf ($3.4 \pm 0.5 \text{ Tg yr}^{-1}$). The 2008–2017 interannual
499 variability (Figure 4) all show a minimum in winter. Maximum emissions were observed in late
500 spring, due to the contribution from mineral fertilizer and manure application, in summer, due
501 to influence of livestock housing emissions, and some years both in spring and summer (Makar
502 et al., 2009; Zhu et al., 2013, 2015). A topographical dependence was also seen in midwest
503 emissions that peaked in April, whereas over the rest of the US maximum emissions were
504 appeared in summer (Paulot et al., 2014).

Deleted: Figure 4

505 Ammonia emissions have different characteristics in South America and in Western
506 Africa as both are fire-dominated regions. For simplicity we only present South America in
507 Figure 4. This region is dominated by natural ammonia emissions mainly from forest, savanna
508 and agricultural fires (Whitburn et al., 2014, 2016b) and volcanoes (Kajino et al., 2004;
509 Uematsu et al., 2004). This causes a strong seasonal variability in the ammonia emissions with
510 the largest fluxes observed from August to October in all years (Figure 4). This strong
511 dependence of South America from biomass burning emissions was first highlighted by Chen
512 et al. (2013) and by van Marle et al. (2017). It also became particularly pronounced during the
513 large wildfires in the Amazon rainforest in summer 2019 (Escobar, 2019). We estimated the
514 10-year average ammonia emissions to be $28 \pm 3.0 \text{ Tg yr}^{-1}$ (average \pm sd) in agreement with
515 VD0.5 (22 Tg yr^{-1}) and VDgrlf ($24 \pm 1.3 \text{ Tg yr}^{-1}$). The respective emissions in EGG are four
516 times lower than these estimates ($7.1 \pm 0.3 \text{ Tg yr}^{-1}$).

Deleted: Figure 4

Deleted: Figure 4

517 The last column to the right of Figure 4 presents the 10-year average annual ammonia
518 emissions and their respective interannual variability in Southeastern Asia. We define this
519 region spanning from 70°E – 130°E in longitude and from 0°N – 45°N in latitude. Ammonia
520 emissions were estimated to be $38 \pm 2.8 \text{ Tg yr}^{-1}$ (average \pm sd) similar to VD0.5 (36 Tg yr^{-1}) and
521 VDgrlf ($39 \pm 1.8 \text{ Tg yr}^{-1}$) and slightly higher than those presented in EGG ($25 \pm 1.2 \text{ Tg yr}^{-1}$). They
522 comprise ammonia fertilizer plants, such as in Pingsongxiang, Shizuishan, Zezhou-Gaoping,
523 Chaerhan Salt Lake, Delingha, Midong-Fukang and Wucaiwan (China), Indo-Gangetic Plain
524 (Pakistan and India), Gresik (Indonesia). China and India contribute more than half of total
525 global ammonia emissions since the 1980s with the majority of these emissions to originate
526 from rice cultivation followed by corn and wheat (crop-specific emissions). More specifically,
527 emissions from these crops due to synthetic fertilizer and livestock manure applications are
528 concentrated in North China Plain (Xu et al., 2018). Considering that Southeastern Asia is the
529 largest agricultural contributor in the global ammonia budget, a strong seasonality in the

Deleted: Figure 4

534 emissions was observed. Temporal ammonia emissions peak in late summer of most years,
535 when emissions from rice cultivation, synthetic fertilizer application and livestock manure
536 spreading (Xu et al., 2016) are important, and in spring when wheat cultivation dominates
537 (Datta et al., 2012). Of course, the respective emissions from biomass burning should also be
538 mentioned. However, these are difficult to be distinguish and are expected to be a relatively
539 small source compared to agricultural emissions.

540 4 Discussion

541 In this section, we conduct simulations over the 10-year period (2008–2017, 1-year spin-
542 up), with all the emissions derived and compare the NH₃ concentrations with ground-based
543 observations over Europe, North America, Southeastern Asia (section 4.1), and observations
544 from CrIS (section 4.1). These simulations consist in: (i) a simulation using traditional
545 emissions using EGG; (ii) a simulation using emissions calculated from IASI data from Van
546 Damme et al. (2018) applying a constant lifetime of 12 hours for ammonia (VD0.5); (iii) a
547 simulation using gridded emissions presented in the present paper (NE) calculated as described
548 in section 2; and (iv) a simulation using emissions calculated from IASI data from Van Damme
549 et al. (2018) applying a variable (modelled) lifetime (VDgrlf). Finally, we perform a sensitivity
550 analysis in order to define the levels of uncertainty of our emissions in section 4.2, and discuss
551 potential limitation of the present study in section 4.3.

552 4.1 Validation against ground-based observations and satellite products

553 **Figure 5** shows a comparison between modelled surface concentrations of ammonia with
554 ground measurements from Europe (EMEP, <https://emep.int/mscw/>), North America (AMoN,
555 <http://nadp.slh.wisc.edu/data/AMoN/>) and Southeastern Asia (EANET,
556 <https://www.eanet.asia>). To avoid overplotting, the Gaussian kernel density estimation (KDE)
557 was used, which is a non-parametric way to estimate the probability density function (PDF) of
558 a random variable (Parzen, 1962):

$$559 \quad f(x) = \frac{1}{Nh} \sum_{i=1}^N K\left(\frac{x-x_i}{h}\right) \quad \text{Eq. 7}$$

560 where K is the kernel, x_i the univariate independent and identically distributed point of the
561 relationship between modelled and measured ammonia and h is a smoothing parameter called
562 the bandwidth. KDE is a fundamental data smoothing tool that attempts to infer characteristics
563 of a population, based on a finite dataset. It weighs the distance of all points in each specific
564 location along the distribution. If there are more points grouped locally, the estimation is higher
565 as the probability of seeing a point at that location increases. The kernel function is the specific

Deleted:

Deleted: 4.2

Deleted: 4.3

Deleted: 4.4

Formatted: Font: Bold

Deleted: Figure 5

571 mechanism used to weigh the points across the data set and it uses the bandwidth to limit the
 572 scope of the function. The latter is computed using the Scott's factor (Scott, 2015). We also
 573 provide the mean fractional bias (MFB) for modelled and measured concentrations of ammonia
 574 as follows:

$$MFB = \frac{1}{N} \frac{\sum_{i=1}^N (C_m - C_o)}{\sum_{i=1}^N \frac{C_m + C_o}{2}} \times 100\% \quad \text{Eq. 8}$$

576 where C_m and C_o are the modelled and measured ammonia concentrations and N is the total
 577 number of observations. MFB is a symmetric performance indicator that gives equal weights
 578 to under- or over-estimated concentrations (minimum to maximum values range from -200%
 579 to 200%). Furthermore, we assess the deviation of the data from the line of best fit using the
 580 root mean square error (RMSE) defined as:

$$RMSE = \sqrt{\frac{\sum_{i=1}^N (C_m - C_o)^2}{N}} \quad \text{Eq. 9}$$

582 From 134 European stations, nearly 300,000 measurements made at a daily to weekly
 583 temporal resolution over the period of study (2007–2018) are presented on **Figure 5**. All
 584 emission datasets underestimate ammonia surface concentration over Europe. The most
 585 accurate prediction of concentrations was achieved using the traditional EGG emissions that
 586 underestimated observations by 67%, also being the least scattered from the best fit
 587 ($RMSE_{EGG} = 4.06 \mu g N m^{-3}$), followed by the emissions presented in this paper ($MFB_{NE} =$
 588 -72% , $RMSE_{NE} = 4.65 \mu g N m^{-3}$), although they were more variable. VD0.5 or VDgrlf
 589 emissions further underestimated observations, though they were less sparse (**Figure 5d**). About
 590 12% of the modelled concentrations using EGG were outside of the 10-fold limit from the
 591 observations, in contrast to only 17% and 15% in VD0.5 and VDgrlf, and 20% in NE. With
 592 regards to the spatial comparison with the observed concentrations, all datasets cause
 593 overestimations in the ammonia concentrations predicted in **Western Europe**, EGG appears to
 594 be the most accurate in Central Europe (all stations with suffix DE00), NE emissions in all
 595 Spanish stations (suffix ES00) and VD0.5 and VDgrlf emissions in Italian stations (**Figure 5**
 596 **7**).

597 The comparison of simulated ammonia concentrations to observations over North
 598 America includes 119 stations, which represent nearly 27,000 observations (**Figure 6**) with a
 599 weekly, bi-weekly or monthly resolution. The only emission dataset that lead to an
 600 underestimation of ammonia concentrations was EGG ($MFB_{EGG} = -28\%$). Two others,
 601 VD0.5 and VDgrlf caused ammonia observations to be strongly overestimated ($MFB_{VD0.5} =$

Formatted: Font: Bold

Deleted: Figure 5

Deleted: Figure 5

Deleted: Eastern

Deleted: (station AM0001R)

Formatted: Font: Bold

Deleted: Figure 5 7

Formatted: Font colour: Black, Shadow

Deleted: Figure 6

608 **52% and $MFB_{VDgrlf} = 54%$**), while NE slightly ($MFB_{NE} = 32%$). All inventories resulted
609 in about the same variability in ammonia concentrations with RMSEs between 4.15 and 4.17
610 $\mu\text{g N m}^{-3}$ (Figure 6). About 10% of the predicted concentrations using EGG emissions were at
611 least 10 times off from the measured ones, more than twice the number of measurements
612 compared to the other dataset. NE emissions better capture levels in the easternmost stations of
613 the US (AL99, AR15, CT15, IL37, IN22, MI52, NY56, ON26) and in California (CA83) and
614 Oklahoma (OK98), which are close to hot-spot regions (see section 3.4). EGG emissions
615 perform better in Northwestern (ID03), Central (KS03) and several stations located over the
616 Eastern United States (KY03, KY98, OH09, AR03, IL46, KS03, GA41). The emission
617 inventory VD0.5 leads to a very good agreement in ammonia concentrations over all stations
618 of the North American continent (AL99, GA40, ID03, GA41, IL37, IL46, IN20, IN22, KS97,
619 PA00, MD99, MI52, TN04, NM99, NY96, OH99, OK98) (Figure S 8).

620 In Southeastern Asia 62 stations from 13 countries were included in the comparison from
621 the EANET monitoring network (Figure 7). These included about 8,000 surface measurements
622 in monthly or 2-weekly resolution. As a whole, all emission inventories underestimate station
623 concentrations of EANET with MFBs between -102% (EGG) and -61% (VD0.5 and VDgrlf).
624 The least spread model concentrations were those simulated using VD0.5 and VDgrlf
625 ($RMSE = 4.61 - 4.65 \mu\text{g N m}^{-3}$). Around 19% of model concentrations using EGG were
626 outside the 10-fold limit of the 1×1 line with observations, 12% using NE emissions and only
627 5% and 6% using VD0.5 and VDgrlf, respectively. VD0.5 and VDgrlf emissions capture well
628 the Japanese (suffix JPA) and Taiwanese stations (suffix THA). Given the short lifetime and
629 the relatively coarse spatial scales, the model fails to capture the variability that exists within
630 each gridbox (Figure S 9).

631 To give an overview of the comparison of the modelled surface concentrations of
632 ammonia from the four different simulations, each with different emissions (EGG, VD0.5, NE
633 and VDgrlf), we present station-by-station calculated MFB values in Figure 8. Although the
634 traditional EGG emissions capture many stations very well, there are large MFB values
635 observed in Eastern and Western USA (AMoN), Northern Europe (EMEP), whereas large
636 overestimations are observed in most of the Southeastern Asian stations (EANET). The large
637 bias at several AMoN stations decrease when using satellite-derived emissions. All datasets
638 miscalculated surface concentrations in Southeastern Asia, although some stations present
639 lower MFBs when using IASI constrained emissions. Note that large differences when

Formatted: Font: Font colour: Black, Text Outline, Shadow

Deleted: Figure 6

Deleted: Figure S 8

Formatted: Font: Font colour: Black, Text Outline, Shadow

Deleted: Figure 7

Deleted: between

Deleted: Figure S 9

Formatted: Font: 12 pt, Not Bold, Font colour: Black, Text Outline, Shadow

Formatted: Body, Space After: 10 pt

Formatted: Font: (Default) Times New Roman, Font colour: Text 1, Shadow

645 comparing bias from all measurements versus station-by-station bias have been calculated as a
646 result of the different frequency of measurements in each station.

647 To further show whether the satellite-derived emissions presented here (NE) capture
648 surface concentrations of ammonia or not, we used surface ammonia concentrations from CrIS
649 from 1st May 2012 to 31st December 2017. The comparison is shown as PDF of surface
650 modelled against CrIS concentrations of ammonia calculated with the Gaussian KDE for North
651 America, Europe and Southeastern Asia in Figure 98. NE emissions slightly overestimate
652 ammonia ($MFB = 0.09 - 0.10$). NE emissions generally result in higher surface
653 concentrations, also showing large RMSEs ($3.28 - 3.51 \mu\text{g N m}^{-3}$). However, 90% of the
654 modelled concentrations were within a factor of 10 from the CrIS observation.

655 4.2 Uncertainty analysis

656 A sensitivity analysis in order to calculate the level of uncertainty that each of the
657 parameter gives to the modelled surface concentrations of ammonia was also performed. The
658 relative uncertainty was calculated as the standard deviation of ammonia's surface
659 concentrations from a model ensemble of 10 members (Table 1) divided by the average. The
660 first six members are the surface concentrations that resulted from simulations of ammonia
661 emissions after perturbation of the Euclidian distance d_k in the parameters of the IDW
662 interpolation. The remaining four members are simulated concentrations using the previously
663 reported emissions datasets (EGG, VD0.5, NE and VDgrlf). The results are shown as a 10-year
664 (2008–2017) annual average relative uncertainty in Figure 109, and as annual average relative
665 uncertainty of surface concentrations for every year of the 10-year period in Figure S 10.

666 The surface concentrations resulting from the different calculated emissions mainly
667 affects oceanic regions, with values reaching 100%. The reason for this could be threefold.
668 First, the IDW interpolation shows to be affected by severe outlier values, which are found in
669 several oceanic regions (Figure S 11); this creates high gridded column ammonia
670 concentrations and, in turn, fluxes at regions that are not supported by previous findings or
671 measurements. Second, the methodology with which ammonia concentrations are retrieved in
672 IASI has certain limitation, with respect to (i) the use of constant vertical profiles for ammonia,
673 (ii) potential dependencies of total column ammonia and temperature that are not taken into
674 account, and (iii) instrumental noise that can cause bias (Whitburn et al., 2016a). Third, there
675 is much less ammonia over the Ocean, hence the relative error bars are much larger. Large
676 uncertainties in surface ammonia concentrations were observed in regions characterized by

Deleted: <#>Validation against satellite products
Here

Deleted: <#> and we compared them with modelled
ammonia concentrations using four emissions datasets
(EGG, VD0.5, NE and VDgrlf), like in the previous section
but in global scale

Deleted: <#>Figure 8

Deleted: <#>A total of 4.5 million surface measurements
were used in the comparison with a global coverage. All
datasets underestimated surface concentrations except

Deleted: <#>, which

Deleted: <#>+

Deleted: <#>48

Deleted: <#>The best fit was achieved for the VDgrlf
emissions, which slightly underestimate ammonia ($MFB =$
 -0.37), while 82% of the measurements were within one
order of magnitude from the 1×1 line, which is also shown
by the small RMSE. VD0.5 emissions produced similar
concentrations, with respect to the RMSE and MFB values,
whereas 79% of them were less than a 10-fold difference
from the observations.

Deleted: <#>r

Formatted: Superscript

Deleted: <#>

Deleted: <#>In general, a better agreement for the most
recent years 2015 – 2017 was achieved. The baseline EGG
emissions resulted in significantly larger deviations of
modelled surface concentrations of ammonia from the CrIS
observations, as shown in Figure 8 comprising the largest
RMSE and MFB values

Deleted: Table 1

Deleted: Figure 9

Deleted: Figure S 10

Deleted: Figure S 11

710 large anthropogenic contribution, such as North India, North China Plain and Central USA.
711 Smaller uncertainties were found in Central Africa and in Amazonia, regions that are linked
712 with episodic biomass burning emissions (Figure 4).

Deleted: Figure 4

713 4.3 Limitations of the present study

714 We discuss the importance of certain limitations in the methodology of the present study
715 and in the validation of the results. These limitations will also be commented upon in the overall
716 conclusion of the paper.

717 Regarding the methodology, emissions of short-lived species are determined, among
718 other methods, using top-down approaches. When only satellite measurements are available,
719 they are usually averaged over a particular location and surface emissions are calculated using
720 a mass balance approach (Lin et al., 2010; Zhao and Wang, 2009). This is done by assuming a
721 1-dimensional box-model, where atmospheric transport between grids is assumed to be
722 negligible and loss due to deposition or chemical reactions very fast. The solution to this
723 problem is the use of Kernels (Boersma et al., 2008), which makes the computation of the
724 emissions very intense. It has been reported that for resolutions, such as those used in the
725 present paper ($2.5^{\circ}\times 1.3^{\circ}$), non-local contributions to the ammonia emissions are relatively
726 small (Turner et al., 2012). Although, the use of Kernels is the proper way to account for non-
727 local contributions, we believe that negligible transport here is a fair assumption, due to the
728 small lifetimes of ammonia calculated from the CTM (11.6 ± 0.6 hours); therefore,
729 transportation from the adjacent grid-cells should be small. Note that although this method has
730 been suggested for short lived climate pollutants, it is not suitable for species with lifetime from
731 days to weeks (e.g. black carbon, Bond et al., 2013).

732 Another limitation of the present study is that the same model is used for the calculation
733 of the modelled lifetimes and for the validation of the emissions that were calculated using
734 these lifetimes (NE and VDgrlf). A more accurate validation would require an independent
735 model for the simulations of surface concentrations using these emissions. Nevertheless, the
736 IASI-constrained emissions of ammonia presented here are publicly available for use in global
737 models.

738 5 Conclusions

739 In the present paper, satellite measurements from IASI were used to constrain global
740 ammonia emissions over the period 2008–2017. The data were firstly processed to monthly
741 ammonia column concentrations with a spatial resolution of $2.5^{\circ}\times 1.3^{\circ}$. Then, using gridded

lifetime for ammonia calculated with a CTM, monthly fluxes were derived. This contrasts with previously reported methods that used a single constant lifetime. This enables a more accurate calculation in regions where different abundances of atmospheric sulfuric and nitric acid, as well as in their precursors (sulfur and nitrogen dioxide, respectively) can neutralize ammonia through heterogeneous chemical reactions to sulfate and nitrate aerosols. The calculated ammonia emission fluxes were then used to simulate ammonia concentrations for the period 2008–2017 (referred to as NE). The same simulations were repeated using baseline emissions from ECLIPSEv5-GFED4-GEIA (referred to as EGG), emissions constrained by Van Damme et al. (2018) IASI data using a constant lifetime for ammonia (named as VD0.5) and emissions based on Van Damme et al. (2018) retrievals using a modelled lifetime from a CTM (named as VDgrlf). The simulated surface concentrations of ammonia were compared with ground measurements over Europe (EMEP), North America (AMoN) and Southeastern Asia (EANET), as well as with global satellite measurements from CrIS. The main conclusions can be summarized as follows:

- The 10-year average annual ammonia emissions calculated here (NE) were estimated to be $213 \pm 18.1 \text{ Tg yr}^{-1}$, which is 15% higher than those in VD0.5 (189 Tg yr^{-1}), and 6% higher than those in VDgrlf ($201 \pm 10.4 \text{ Tg yr}^{-1}$). These emission values amount to twice the published from datasets, such as EGG ($65 \pm 2.8 \text{ Tg yr}^{-1}$) and EDGARv4.3.1-GFED4, ($103 \pm 5.5 \text{ Tg yr}^{-1}$).
- In the North China Plain, a region characterized by intensive agricultural activities, a small increase of ammonia emissions is simulated after 2015. This is attributed to decreases in sulfur species, as revealed from OMI and MERRA-2 measurements. Less sulfates in the atmosphere leads to less ammonia neutralization and hence to larger loads in the atmospheric column as measured by IASI.
- In Europe, the 10-year average of ammonia emissions were estimated at $15 \pm 2.2 \text{ Tg yr}^{-1}$ (NE), twice as much as those in EGG ($6.9 \pm 1.1 \text{ Tg yr}^{-1}$) and similar to those in VD0.5 (11 Tg yr^{-1}) or VDgrlf ($11 \pm 1.0 \text{ Tg yr}^{-1}$). The strongest emission fluxes were calculated over Belgium, Netherlands, Italy (Po Valley), Northwestern Germany and Denmark. These regions are known for industrial and agricultural applications, animal breeding activities, manure/slurry storage facilities and manure/slurry application to soils.
- Some hot-spot regions with high ammonia emissions were distinguished in North America: (i) in Colorado, due to large agricultural activity, (ii) in Iowa, northern Texas and Kansas, due to animal breeding, (iii) in Salt Lake, Cache, and Utah, due to animal farms associated

776 with open waste pits and (iv) in California, due to animal breeding and agricultural
777 practices. Ammonia emissions in North America were $1.1 \pm 0.1 \text{ Tg yr}^{-1}$ or two orders of
778 magnitude higher than in EGG ($6.2 \pm 0.1 \text{ kt yr}^{-1}$) and three times lower than those in VD0.5
779 (3.1 Tg yr^{-1}) or in VDgrlf ($3.4 \pm 0.5 \text{ Tg yr}^{-1}$), with maxima observed in late spring, due to
780 fertilization and manure application and summer, due to livestock emissions.

781 • South America is dominated by natural ammonia emissions mainly from forest, savanna
782 and agricultural fires causing a strong seasonality with the largest fluxes between August
783 and October. The 10-year average ammonia emissions were as high as $28 \pm 3.0 \text{ Tg yr}^{-1}$
784 similar to VD0.5 (22 Tg yr^{-1}) and VDgrlf ($24 \pm 1.3 \text{ Tg yr}^{-1}$) and four times higher than EGG
785 ($7.1 \pm 0.3 \text{ Tg yr}^{-1}$).

786 • In Southeastern Asia, the 10-year average ammonia emissions were $38 \pm 2.8 \text{ Tg yr}^{-1}$, in
787 agreement with VD0.5 (36 Tg yr^{-1}) and VDgrlf ($39 \pm 1.8 \text{ Tg yr}^{-1}$) and slightly higher than
788 those in EGG ($25 \pm 1.2 \text{ Tg yr}^{-1}$). The main sources were from fertilizer plants in China,
789 Pakistan, India and Indonesia. China and India hold the largest share in the ammonia
790 emissions mainly due to rice, corn and wheat cultivation. A strong seasonality in the
791 emissions was observed with a late summer peak in most years, due to rice cultivation,
792 synthetic fertilizer and livestock manure applications and in spring due to wheat
793 cultivation.

794 • Large bias was calculated in several ground-based stations when using the state-of-the-art
795 emissions EGG. The bias decreased substantially when satellite-derived emissions were
796 used to simulate surface concentrations of ammonia.

798 *Data availability.* All data and python scripts used for the present publication are open through
799 the web address <https://folk.nilu.no/~nikolaos/acp-2020-1008/> or can be obtained from the
800 corresponding author upon request.

802 *Competing interests.* The authors declare no competing interests.

803 *Acknowledgements.* This study was supported by the Research Council of Norway (project
804 ID: 275407, COMBAT – Quantification of Global Ammonia Sources constrained by a
805 Bayesian Inversion Technique). Lieven Clarisse and Martin Van Damme are respectively a
806 research associate and a postdoctoral researcher supported by the F.R.S.–FNRS.
807
808

Formatted: Indent: Left: 0.12 cm, Bulleted + Level: 1 +
Aligned at: 0.63 cm + Indent at: 1.27 cm

Deleted: About 88% of the modelled concentrations over Europe using EGG were inside the 10-fold limit from the observations, higher than those with VD0.5 (83%), VDgrlf (85%) and NE (80%). All emission datasets overestimate of ammonia in Eastern Europe, EGG captures better Central Europe, NE emissions predict concentrations in Spain and VD0.5 with VDgrlf emissions in Italy.[†] In North America, 90% of the modelled concentrations using EGG emissions were less than 10 times different from the measured ones; more than 95% of the modelled concentrations in North American stations were in the same range using NE, VD0.5 and VDgrlf emissions. NE emissions better capture levels in the easternmost stations of the US closer to the respective hot-spot regions, whereas EGG emissions perform better in Northwestern and Central USA. VD0.5 and VDgrlf emissions perform well in most of the North American stations.[‡] All emissions underestimate station concentrations in Southeastern Asia. The least spread model concentrations were those simulated using VD0.5 and VDgrlf. About 81% of modelled concentrations using EGG were in the 10-fold limit of the 1×1 line with observations, 88% using NE and only 95% and 94% using VD0.5 and VDgrlf, respectively. VD0.5 and VDgrlf emissions capture well the Japanese and Taiwanese stations.[§] The comparison of the modelled ammonia with satellite observations from CrIS globally showed that the best agreement was achieved using the VDgrlf emissions in 2012–2014. After 2015, all satellite retrieved emissions show a better agreement with CrIS concentrations.[¶] Overall, the satellite-constrained ammonia emissions calculated using a variable lifetime appear to give more realistic concentrations, with respect to station and satellite measurements. Accordingly, state-of-the-art emissions appear to underestimate ammonia significantly.

Deleted: <https://folk.nilu.no/~nikolaos/AMMONIA/>

845 *Author contributions.* N.E. performed the simulations, analyses, wrote and coordinated the
846 paper. S.E. contributed to the lifetime calculations. Y.B., D.H. and A.C. set up the CTM model.
847 M.V.D., P.-F.C. and L.C. provided the IASI data, while M.W.S. and K.E.C.-P. provided the
848 observations from CrIS. All authors contributed to the final version of the manuscript.

849

850 **References**

- 851 Abbatt, J. P. D., Benz, S., Cziczo, D. J., Kanji, Z., Lohmann, U. and Mohler, O.: Solid
852 Ammonium Sulfate Aerosols as Ice Nuclei: A Pathway for Cirrus Cloud Formation,
853 *Science* (80-.), (September), 1770–1773, 2006.
- 854 Anderson, N., Strader, R. and Davidson, C.: Airborne reduced nitrogen: Ammonia
855 emissions from agriculture and other sources, *Environ. Int.*, 29(2–3), 277–286,
856 doi:10.1016/S0160-4120(02)00186-1, 2003.
- 857 Aneja, V. P., Schlesinger, W. H. and Erisman, J. W.: Farming pollution, *Nat. Geosci.*,
858 1(7), 409–411 [online] Available from: <http://dx.doi.org/10.1038/ngeo236>, 2008.
- 859 Aneja, V. P., Schlesinger, W. H. and Erisman, J. W.: Effects of agriculture upon the
860 air quality and climate: Research, policy, and regulations, *Environ. Sci. Technol.*,
861 43(12), 4234–4240, doi:10.1021/es8024403, 2009.
- 862 August, T., Klaes, D., Schlüssel, P., Hultberg, T., Crapeau, M., Arriaga, A., O’Carroll,
863 A., Coppens, D., Munro, R. and Calbet, X.: IASI on Metop-A: Operational Level 2
864 retrievals after five years in orbit, *J. Quant. Spectrosc. Radiat. Transf.*, 113(11),
865 1340–1371, doi:10.1016/j.jqsrt.2012.02.028, 2012.
- 866 Behera, S. N., Sharma, M., Aneja, V. P. and Balasubramanian, R.: Ammonia in the
867 atmosphere: A review on emission sources, atmospheric chemistry and deposition
868 on terrestrial bodies, *Environ. Sci. Pollut. Res.*, 20(11), 8092–8131,
869 doi:10.1007/s11356-013-2051-9, 2013.
- 870 Boersma, K. F., Jacob, D. J., Bucsel, E. J., Perring, A. E., Dirksen, R., van der A, R.
871 J., Yantosca, R. M., Park, R. J., Wenig, M. O., Bertram, T. H. and Cohen, R. C.:
872 Validation of OMI tropospheric NO₂ observations during INTEX-B and application to
873 constrain NO_x emissions over the eastern United States and Mexico, *Atmos.*
874 *Environ.*, 42(19), 4480–4497, doi:10.1016/j.atmosenv.2008.02.004, 2008.
- 875 Bond, T. C., Doherty, S. J., Fahey, D. W., Forster, P. M., Berntsen, T., Deangelo, B.
876 J., Flanner, M. G., Ghan, S., Kärcher, B., Koch, D., Kinne, S., Kondo, Y., Quinn, P.
877 K., Sarofim, M. C., Schultz, M. G., Schulz, M., Venkataraman, C., Zhang, H., Zhang,
878 S., Bellouin, N., Guttikunda, S. K., Hopke, P. K., Jacobson, M. Z., Kaiser, J. W.,
879 Klimont, Z., Lohmann, U., Schwarz, J. P., Shindell, D., Storelvmo, T., Warren, S. G.
880 and Zender, C. S.: Bounding the role of black carbon in the climate system: A
881 scientific assessment, *J. Geophys. Res. Atmos.*, 118(11), 5380–5552,
882 doi:10.1002/jgrd.50171, 2013.
- 883 Bouwman, A. F., Lee, D. S., Asman, W. A. H., Dentener, F. J., Van Der Hoek, K. W.
884 and Olivier, J. G. J.: A global high-resolution emission inventory for ammonia, *Global*
885 *Biogeochem. Cycles*, 11(4), 561–587, doi:10.1029/97GB02266, 1997.
- 886 Cao, H., Henze, D. K., Shephard, M. W., Damers, E., Cady-Pereira, K., Alvarado,
887 M., Lonsdale, C., Luo, G., Yu, F., Zhu, L., Danielson, C. G. and Edgerton, E. S.:
888 Inverse modeling of NH₃ sources using CrIS remote sensing measurements,
889 *Environ. Res. Lett.*, in press, doi:10.1088/1748-9326/abb5cc, 2020.
- 890 Chen, Y., Morton, D. C., Jin, Y., Gollatz, G. J., Kasibhatla, P. S., Van Der Werf, G.
891 R., Defries, R. S. and Randerson, J. T.: Long-term trends and interannual variability
892 of forest, savanna and agricultural fires in South America, *Carbon Manag.*, 4(6), 617–

893 638, doi:10.4155/cmt.13.61, 2013.
894 Clarisse, L., Clerbaux, C., Dentener, F., Hurtmans, D. and Coheur, P.-F.: Global
895 ammonia distribution derived from infrared satellite observations, *Nat. Geosci*, 2(7),
896 479–483 [online] Available from: <http://dx.doi.org/10.1038/ngeo551>, 2009.
897 Clarisse, L., Shephard, M. W., Dentener, F., Hurtmans, D., Cady-Pereira, K.,
898 Karagulian, F., Van Damme, M., Clerbaux, C. and Coheur, P. F.: Satellite monitoring
899 of ammonia: A case study of the San Joaquin Valley, *J. Geophys. Res.*, 115,
900 doi:10.1029/2009jd013291, 2010.
901 Clerbaux, C., Boynard, A., Clarisse, L., George, M., Hadji-Lazaro, J., Herbin, H.,
902 Hurtmans, D., Pommier, M., Razavi, A., Turquety, S., Wespes, C. and Coheur, P.-F.:
903 Monitoring of atmospheric composition using the thermal infrared IASI/MetOp
904 sounder, *Atmos. Chem. Phys.*, 9(16), 6041–6054, doi:10.5194/acp-9-6041-2009,
905 2009.
906 De Cort, M., Dubois, G., Fridman, S. D., Germenchuk, M., G., Izrael, Y. A., Janssens,
907 A., Jones, A. R., Kelly, G., N., Kvasnikova, E., V., Matveenko, I., I., Nazarov, I., N.,
908 Pokumeiko, Y., M., Sitak, V. A., Stukin, E., D., Tabachny, L., Y., Tsaturov, Y. S. and
909 Avdyushin, S., I.: Atlas of caesium deposition on Europe after the Chernobyl
910 accident, EU - Office for Official Publications of the European Communities,
911 Luxembourg., 1998.
912 Crippa, M., Janssens-Maenhout, G., Dentener, F., Guizzardi, D., Sindelarova, K.,
913 Muntean, M., Van Dingenen, R. and Granier, C.: Forty years of improvements in
914 European air quality: Regional policy-industry interactions with global impacts,
915 *Atmos. Chem. Phys.*, 16(6), 3825–3841, doi:10.5194/acp-16-3825-2016, 2016.
916 Croft, B., Pierce, J. R. and Martin, R. V.: Interpreting aerosol lifetimes using the
917 GEOS-Chem model and constraints from radionuclide measurements, *Atmos. Chem.*
918 *Phys.*, 14(8), 4313–4325, doi:10.5194/acp-14-4313-2014, 2014.
919 Van Damme, M., Wichink Kruit, R. J., Schaap, M., Clarisse, L., Clerbaux, C., Coheur,
920 P. F., Dammers, E., Dolman, A. J. and Erisman, J. W.: Evaluating 4 years of
921 atmospheric ammonia (NH₃) over Europe using IASI satellite observations and
922 LOTOS-EUROS model results, *J. Geophys. Res. Atmos.*, 119(15), 9549–9566,
923 doi:10.1002/2014JD021911, 2014a.
924 Van Damme, M., Clarisse, L., Heald, C. L., Hurtmans, D., Ngadi, Y., Clerbaux, C.,
925 Dolman, A. J., Erisman, J. W. and Coheur, P. F.: Global distributions, time series and
926 error characterization of atmospheric ammonia (NH₃) from IASI satellite
927 observations, *Atmos. Chem. Phys.*, 14(6), 2905–2922, doi:10.5194/acp-14-2905-
928 2014, 2014b.
929 Van Damme, M., Clarisse, L., Dammers, E., Liu, X., Nowak, J. B., Clerbaux, C.,
930 Flechard, C. R., Galy-Lacaux, C., Xu, W., Neuman, J. A., Tang, Y. S., Sutton, M. A.,
931 Erisman, J. W. and Coheur, P. F.: Towards validation of ammonia (NH₃)
932 measurements from the IASI satellite, *Atmos. Meas. Tech.*, 8(3), 1575–1591,
933 doi:10.5194/amt-8-1575-2015, 2015.
934 Van Damme, M., Whitburn, S., Clarisse, L., Clerbaux, C., Hurtmans, D. and Coheur,
935 P.: Version 2 of the IASI NH₃ neural network retrieval algorithm : near-real-time and
936 reanalysed datasets, , 4905–4914, 2017.
937 Van Damme, M., Clarisse, L., Whitburn, S., Hadji-Lazaro, J., Hurtmans, D., Clerbaux,
938 C. and Coheur, P.-F.: Industrial and agricultural ammonia point sources exposed,
939 *Nature*, 564(7734), 99–103, doi:10.1038/s41586-018-0747-1, 2018.
940 Dammers, E., Palm, M., Van Damme, M., Vigouroux, C., Smale, D., Conway, S.,
941 Toon, G. C., Jones, N., Nussbaumer, E., Warneke, T., Petri, C., Clarisse, L.,
942 Clerbaux, C., Hermans, C., Lutsch, E., Strong, K., Hannigan, J. W., Nakajima, H.,

943 Morino, I., Herrera, B., Stremme, W., Grutter, M., Schaap, M., Kruit, R. J. W., Notholt,
944 J., Coheur, P. F. and Erisman, J. W.: An evaluation of IASI-NH 3 with ground-based
945 Fourier transform infrared spectroscopy measurements, *Atmos. Chem. Phys.*,
946 16(16), 10351–10368, doi:10.5194/acp-16-10351-2016, 2016.

947 Dammers, E., Shephard, M. W., Palm, M., Cady-pereira, K., Capps, S., Lutsch, E.,
948 Strong, K., Hannigan, J. W., Ortega, I., Toon, G. C., Stremme, W. and Grutter, M.:
949 Validation of the CrIS fast physical NH 3 retrieval with ground-based FTIR, , 87,
950 2645–2667, 2017.

951 Dammers, E., McLinden, C. A., Griffin, D., Shephard, M. W., Van Der Graaf, S.,
952 Lutsch, E., Schaap, M., Gainairu-Matz, Y., Fioletov, V., Van Damme, M., Whitburn,
953 S., Clarisse, L., Cady-Pereira, K., Clerbaux, C., Francois Coheur, P. and Erisman, J.
954 W.: NH3 emissions from large point sources derived from CrIS and IASI satellite
955 observations, *Atmos. Chem. Phys.*, 19(19), 12261–12293, doi:10.5194/acp-19-
956 12261-2019, 2019.

957 Datta, A., Sharma, S. K., Harit, R. C., Kumar, V., Mandal, T. K. and Pathak, H.:
958 Ammonia emission from subtropical crop land area in india, *Asia-Pacific J. Atmos.*
959 *Sci.*, 48(3), 275–281, doi:10.1007/s13143-012-0027-1, 2012.

960 Dee, D. P., Uppala, S. M., Simmons, A. J., Berrisford, P., Poli, P., Kobayashi, S.,
961 Andrae, U., Balmaseda, M. A., Balsamo, G., Bauer, P., Bechtold, P., Beljaars, A. C.
962 M., van de Berg, L., Bidlot, J., Bormann, N., Delsol, C., Dragani, R., Fuentes, M.,
963 Geer, A. J., Haimberger, L., Healy, S. B., Hersbach, H., H??lm, E. V., Isaksen, L.,
964 K??lberg, P., K??hler, M., Matricardi, M., McNally, A. P., Monge-Sanz, B. M.,
965 Morcrette, J. J., Park, B. K., Peubey, C., de Rosnay, P., Tavolato, C., Th??paut, J. N.
966 and Vitart, F.: The ERA-Interim reanalysis: Configuration and performance of the
967 data assimilation system, *Q. J. R. Meteorol. Soc.*, 137(656), 553–597,
968 doi:10.1002/qj.828, 2011.

969 Dentener, F. J. and Crutzen, P. J.: A 3-Dimensional Model Of The Global Ammonia
970 Cycle, *J. Atmos. Chem.*, 19(4), 331–369, doi:10.1007/bf00694492, 1994.

971 Duncan, B. N., Lamsal, L. N., Thompson, A. M., Yoshida, Y., Lu, Z., Streets, D. G.,
972 Hurwitz, M. M. and Pickering, K. E.: A space-based, high-resolution view of notable
973 changes in urban NOx pollution around the world (2005–2014), *J. Geophys. Res.*
974 *Ocean.*, 121, 976–996, doi:10.1002/2015JD024121, 2016.

975 Emanuel, K. A.: A Scheme for Representing Cumulus Convection in Large-Scale
976 Models, *J. Atmos. Sci.*, 48(21), 2313–2329, doi:10.1175/1520-
977 0469(1991)048<2313:ASFRCC>2.0.CO;2, 1991.

978 Erisman, J. A. N. W.: The Nanjing Declaration on Management of Reactive Nitrogen,
979 , 54(4), 286–287, 2004.

980 Erisman, J. W., Bleeker, A., Galloway, J. and Sutton, M. S.: Reduced nitrogen in
981 ecology and the environment, *Environ. Pollut.*, 150(1), 140–149,
982 doi:10.1016/j.envpol.2007.06.033, 2007.

983 Escobar, H.: Amazon fires clearly linked to deforestation, scientists say, *Science* (80-
984 .), 365(6456), 853, doi:10.1126/science.365.6456.853, 2019.

985 European Environment Agency: EMEP/EEA air pollutant emission inventory
986 guidebook 2019: Technical guidance to prepare national emission inventories., 2019.

987 Evangeliou, N., Hamburger, T., Talerko, N., Zibtsev, S., Bondar, Y., Stohl, A.,
988 Balkanski, Y., Mousseau, T. A. and Møller, A. P.: Reconstructing the Chernobyl
989 Nuclear Power Plant (CNPP) accident 30 years after. A unique database of air
990 concentration and deposition measurements over Europe, *Environ. Pollut.*, (August),
991 doi:10.1016/j.envpol.2016.05.030, 2016.

992 Faulkner, W. B. and Shaw, B. W.: Review of ammonia emission factors for United

993 States animal agriculture, *Atmos. Environ.*, 42(27), 6567–6574,
994 doi:10.1016/j.atmosenv.2008.04.021, 2008.
995 Flechard, C. R. and Fowler, D.: Atmospheric ammonia at a moorland site. I: The
996 meteorological control of ambient ammonia concentrations and the influence of local
997 sources, *Q. J. R. Meteorol. Soc.*, 124(547), 733–757, doi:10.1256/smsqj.54704,
998 1998.
999 Folberth, G. A., Hauglustaine, D. A., Lathièrre, J. and Brocheton, F.: Interactive
1000 chemistry in the Laboratoire de Météorologie Dynamique general circulation model:
1001 model description and impact analysis of biogenic hydrocarbons on tropospheric
1002 chemistry, *Atmos. Chem. Phys.*, 6(8), 2273–2319, doi:10.5194/acp-6-2273-2006,
1003 2006.
1004 Fowler, D., Muller, J. B. A., Smith, R. I., Dragosits, U., Skiba, U., Sutton, M. A. and
1005 Brimblecombe, P.: A CHRONOLOGY OF NITROGEN DEPOSITION IN THE UK, , 2,
1006 9–23, 2004.
1007 Gelaro, R., McCarty, W., Suárez, M. J., Todling, R., Molod, A., Takacs, L., Randles,
1008 C. A., Darmenov, A., Bosilovich, M. G., Reichle, R., Wargan, K., Coy, L., Cullather,
1009 R., Draper, C., Akella, S., Buchard, V., Conaty, A., da Silva, A. M., Gu, W., Kim, G.
1010 K., Koster, R., Lucchesi, R., Merkova, D., Nielsen, J. E., Partyka, G., Pawson, S.,
1011 Putman, W., Rienecker, M., Schubert, S. D., Sienkiewicz, M. and Zhao, B.: The
1012 modern-era retrospective analysis for research and applications, version 2 (MERRA-
1013 2), *J. Clim.*, 30(14), 5419–5454, doi:10.1175/JCLI-D-16-0758.1, 2017.
1014 Giglio, L., Randerson, J. T. and van der Werf, G. R.: Analysis of daily, monthly, and
1015 annual burned area using the fourth-generation global fire emissions database
1016 (GFED4), *J. Geophys. Res. Biogeosciences*, 118, 317–328, doi:10.1002/jgrg.20042,
1017 2013, 2013.
1018 Gu, B., Sutton, M. A., Chang, S. X., Ge, Y. and Chang, J.: Agricultural ammonia
1019 emissions contribute to China's urban air pollution, *Front. Ecol. Environ.*, 12(5), 265–
1020 266, doi:10.1890/14.WB.007, 2014.
1021 Hauglustaine, D. A., Hourdin, F., Jourdain, L., Filiberti, M.-A., Walters, S., Lamarque,
1022 J.-F. and Holland, E. A.: Interactive chemistry in the Laboratoire de Meteorologie
1023 Dynamique general circulation model: Description and background tropospheric
1024 chemistry evaluation, *J. Geophys. Res.*, 109(D04314), doi:10.1029/2003JD003957,
1025 2004.
1026 Hauglustaine, D. A., Balkanski, Y. and Schulz, M.: A global model simulation of
1027 present and future nitrate aerosols and their direct radiative forcing of climate, *Atmos.*
1028 *Chem. Phys.*, 14(20), 11031–11063, doi:10.5194/acp-14-11031-2014, 2014.
1029 Henze, D. K., Shindell, D. T., Akhtar, F., Spurr, R. J. D., Pinder, R. W., Loughlin, D.,
1030 Kopacz, M., Singh, K. and Shim, C.: Spatially Refined Aerosol Direct Radiative
1031 Forcing Efficiencies, *Environ. Sci. Technol.*, 46, 9511–9518, doi:10.1021/es301993s,
1032 2012.
1033 Hertel, O., Skjoth, C. A., Reis, S., Bleeker, A., Harrison, R. M., Cape, J. N., Fowler,
1034 D., Skiba, U., Simpson, D., Jickells, T., Kulmala, M., Gyldenkerne, S., Sorensen, L.
1035 L., Erisman, J. W. and Sutton, M. A.: Governing processes for reactive nitrogen
1036 compounds in the European atmosphere, *Biogeosciences*, 9(12), 4921–4954,
1037 doi:10.5194/bg-9-4921-2012, 2012.
1038 Hourdin, F. and Armengaud, A.: The Use of Finite-Volume Methods for Atmospheric
1039 Advection of Trace Species. Part I: Test of Various Formulations in a General
1040 Circulation Model, *Mon. Weather Rev.*, 127(5), 822–837, doi:10.1175/1520-
1041 0493(1999)127<0822:TUOFVM>2.0.CO;2, 1999.
1042 Hourdin, F., Musat, I., Bony, S., Braconnot, P., Codron, F., Dufresne, J. L., Fairhead,

1043 L., Filiberti, M. A., Friedlingstein, P., Grandpeix, J. Y., Krinner, G., LeVan, P., Li, Z. X.
1044 and Lott, F.: The LMDZ4 general circulation model: Climate performance and
1045 sensitivity to parametrized physics with emphasis on tropical convection, *Clim. Dyn.*,
1046 27(7–8), 787–813, doi:10.1007/s00382-006-0158-0, 2006.

1047 Hov, Ø., Hjøllø, B. A. and Eliassen, A.: Transport distance of ammonia and
1048 ammonium in Northern Europe: 2. Its relation to emissions of SO₂ and NO_x, *J.*
1049 *Geophys. Res.*, 99(D9), 18749, doi:10.1029/94jd00910, 1994.

1050 Kajino, M., Ueda, H., Satsumabayashi, H. and An, J.: Impacts of the eruption of
1051 Miyakejima Volcano on air quality over far east Asia, *J. Geophys. Res. D Atmos.*,
1052 109(21), 1–11, doi:10.1029/2004JD004762, 2004.

1053 Kean, A. J., Littlejohn, D., Ban-Weiss, G. A., Harley, R. A., Kirchstetter, T. W. and
1054 Lunden, M. M.: Trends in on-road vehicle emissions of ammonia, *Atmos. Environ.*,
1055 43(8), 1565–1570, doi:10.1016/j.atmosenv.2008.09.085, 2009.

1056 Kharol, S. K., Shephard, M. W., McLinden, C. A., Zhang, L., Sioris, C. E., O'Brien, J.
1057 M., Vet, R., Cady-Pereira, K. E., Hare, E., Siemons, J. and Krotkov, N. A.: Dry
1058 Deposition of Reactive Nitrogen From Satellite Observations of Ammonia and
1059 Nitrogen Dioxide Over North America, *Geophys. Res. Lett.*, 45(2), 1157–1166,
1060 doi:10.1002/2017GL075832, 2018.

1061 Klimont, Z., Kupiainen, K., Heyes, C., Purohit, P., Cofala, J., Rafaj, P., Borcken-
1062 Kleefeld, J. and Schöpp, W.: Global anthropogenic emissions of particulate matter
1063 including black carbon, *Atmos. Chem. Phys.*, 17, 8681–8723, doi:10.5194/acp-17-
1064 8681-2017, 2017.

1065 Koukoulis, M. E., Theys, N., Ding, J., Zyrichidou, I., Mijling, B., Balis, D. and Johannes
1066 Van Der A, R.: Updated SO₂ emission estimates over China using OMI/Aura
1067 observations, *Atmos. Meas. Tech.*, 11(3), 1817–1832, doi:10.5194/amt-11-1817-
1068 2018, 2018.

1069 Krinner, G., Viovy, N., de Noblet-Ducoudré, N., Ogée, J., Polcher, J., Friedlingstein,
1070 P., Ciais, P., Sitch, S. and Prentice, I. C.: A dynamic global vegetation model for
1071 studies of the coupled atmosphere-biosphere system, *Global Biogeochem. Cycles*,
1072 19(1), n/a–n/a, doi:10.1029/2003GB002199, 2005.

1073 Krotkov, N. A., McLinden, C. A., Li, C., Lamsal, L. N., Celarier, E. A., Marchenko, S.
1074 V., Swartz, W. H., Bucseles, E. J., Joiner, J., Duncan, B. N., Folkert Boersma, K.,
1075 Pepijn Veefkind, J., Levelt, P. F., Fioletov, V. E., Dickerson, R. R., He, H., Lu, Z. and
1076 Streets, D. G.: Aura OMI observations of regional SO₂ and NO₂ pollution changes
1077 from 2005 to 2015, *Atmos. Chem. Phys.*, 16(7), 4605–4629, doi:10.5194/acp-16-
1078 4605-2016, 2016.

1079 Kuttippurath, J., Singh, A., Dash, S. P., Mallick, N., Clerbaux, C., Van Damme, M.,
1080 Clarisse, L., Coheur, P. F., Raj, S., Abhishek, K. and Varikoden, H.: Record high
1081 levels of atmospheric ammonia over India: Spatial and temporal analyses, *Sci. Total*
1082 *Environ.*, 740, 139986, doi:10.1016/j.scitotenv.2020.139986, 2020.

1083 Lachatre, M., Fortems-Cheiney, A., Foret, G., Siour, G., Dufour, G., Clarisse, L.,
1084 Clerbaux, C., Coheur, P. F., Van Damme, M. and Beekmann, M.: The unintended
1085 consequence of SO₂ and NO₂ regulations over China: Increase of ammonia levels
1086 and impact on PM_{2.5} concentrations, *Atmos. Chem. Phys.*, 19(10), 6701–6716,
1087 doi:10.5194/acp-19-6701-2019, 2019.

1088 Leip, A., Billen, G., Garnier, J., Grizzetti, B., Lassaletta, L., Reis, S., Simpson, D.,
1089 Sutton, M. a, de Vries, W., Weiss, F. and Westhoek, H.: Impacts of European
1090 livestock production: nitrogen, sulphur, phosphorus and greenhouse gas emissions,
1091 land-use, water eutrophication and biodiversity, *Environ. Res. Lett.*, 10(11), 115004,
1092 doi:10.1088/1748-9326/10/11/115004, 2015.

1093 Lelieveld, J., Evans, J. S., Fnais, M., Giannadaki, D. and Pozzer, A.: The contribution
 1094 of outdoor air pollution sources to premature mortality on a global scale., *Nature*,
 1095 525(7569), 367–71, doi:10.1038/nature15371, 2015.
 1096 Li, C., Martin, R. V., Shephard, M. W., Pereira, K. C., Cooper, M. J., Kaiser, J., Lee,
 1097 C. J., Zhang, L. and Henze, D. K.: Assessing the Iterative Finite Difference Mass
 1098 Balance and 4D - Var Methods to Derive Ammonia Emissions Over North America
 1099 Using Synthetic Observations, , 4222–4236, doi:10.1029/2018JD030183, 2019.
 1100 Lin, J. T., McElroy, M. B. and Boersma, K. F.: Constraint of anthropogenic NOx
 1101 emissions in China from different sectors: A new methodology using multiple satellite
 1102 retrievals, *Atmos. Chem. Phys.*, 10(1), 63–78, doi:10.5194/acp-10-63-2010, 2010.
 1103 Liu, F., Beirle, S., Zhang, Q., van der A, R. J., Zheng, B., Tong, D. and He, K.: NOx
 1104 emission trends over Chinese cities estimated from OMI observations during 2005 to
 1105 2015, *Atmos. Chem. Phys. Discuss.*, (2), 1–21, doi:10.5194/acp-2017-369, 2017.
 1106 Liu, M., Huang, X., Song, Y., Xu, T., Wang, S., Wu, Z., Hu, M., Zhang, L., Zhang, Q.,
 1107 Pan, Y. and Zhu, T.: Rapid SO2 emission reductions significantly increase
 1108 tropospheric ammonia concentrations over the North China Plain, *Atmos. Chem.*
 1109 *Phys.*, (18), 17933–17943, doi:10.5194/acp-18-17933-2018, 2018.
 1110 Makar, P. A., Moran, M. D., Zheng, Q., Cousineau, S., Sassi, M., Duhamel, A.,
 1111 Besner, M., Davignon, D., Crevier, L. P. and Bouchet, V. S.: Modelling the impacts of
 1112 ammonia emissions reductions on North American air quality, *Atmos. Chem. Phys.*,
 1113 9(18), 7183–7212, doi:10.5194/acp-9-7183-2009, 2009.
 1114 Malm, W. C.: Spatial and monthly trends in speciated fine particle concentration in
 1115 the United States, *J. Geophys. Res.*, 109(D3), D03306, doi:10.1029/2003JD003739,
 1116 2004.
 1117 Malm, W. C., Schichtel, B. A., Barna, M. G., Gebhart, K. A., Rodriguez, M. A., Collett,
 1118 J. L., Carrico, C. M., Benedict, K. B., Prenni, A. J. and Kreidenweis, S. M.: Aerosol
 1119 species concentrations and source apportionment of ammonia at Rocky Mountain
 1120 National Park, *J. Air Waste Manag. Assoc.*, 63(11), 1245–1263,
 1121 doi:10.1080/10962247.2013.804466, 2013.
 1122 van Marle, M. J. E., Field, R. D., van der Werf, G. R., Estrada de Wagt, I. A.,
 1123 Houghton, R. A., Rizzo, L. V., Artaxo, P. and Tsigaridis, K.: Fire and deforestation
 1124 dynamics in Amazonia (1973–2014), *Global Biogeochem. Cycles*, 31(1), 24–38,
 1125 doi:10.1002/2016GB005445, 2017.
 1126 McQuilling, A. M.: Ammonia emissions from livestock in the United States: From farm
 1127 emissions models to a new national inventory, ProQuest Diss. Theses, 168 [online]
 1128 Available from:
 1129 [https://search.proquest.com/docview/1841254436?accountid=133571%0Ahttp://www](https://search.proquest.com/docview/1841254436?accountid=133571%0Ahttp://www.yidu.edu.cn/educhina/educhina.do?artifact=&svalue=Ammonia+emissions+from+live+stock+in+the+United+States%3A+From+farm+emissions+models+to+a+new+nati on al+inventory&stype=2&s=on%0Ah)
 1130 [.yidu.edu.cn/educhina/educhina.do?artifact=&svalue=Ammonia+emissions+from+live](http://www.yidu.edu.cn/educhina/educhina.do?artifact=&svalue=Ammonia+emissions+from+live+stock+in+the+United+States%3A+From+farm+emissions+models+to+a+new+nati on al+inventory&stype=2&s=on%0Ah)
 1131 [stock+in+the+United+States%3A+From+farm+emissions+models+to+a+new+nati on](http://www.yidu.edu.cn/educhina/educhina.do?artifact=&svalue=Ammonia+emissions+from+live+stock+in+the+United+States%3A+From+farm+emissions+models+to+a+new+nati on al+inventory&stype=2&s=on%0Ah)
 1132 [al+inventory&stype=2&s=on%0Ah](http://www.yidu.edu.cn/educhina/educhina.do?artifact=&svalue=Ammonia+emissions+from+live+stock+in+the+United+States%3A+From+farm+emissions+models+to+a+new+nati on al+inventory&stype=2&s=on%0Ah), 2016.
 1133 Min Hao, W., Petkov, A., Nordgren, B. L., Corley, R. E., Silverstein, R. P., Urbanski,
 1134 S. P., Evangeliou, N., Balkanski, Y. and Kinder, B. L.: Daily black carbon emissions
 1135 from fires in northern Eurasia for 2002-2015, *Geosci. Model Dev.*, 9(12),
 1136 doi:10.5194/gmd-9-4461-2016, 2016.
 1137 Möller, D. and Schieferdecker, H.: A relationship between agricultural NH₃
 1138 emissions and the atmospheric SO₂ content over industrial areas, *Atmos. Environ.*,
 1139 19(5), 695–700, doi:10.1016/0004-6981(85)90056-3, 1985.
 1140 Norman, M. and Leck, C.: Distribution of marine boundary layer ammonia over the
 1141 Atlantic and Indian Oceans during the Aerosols99 cruise, *J. Geophys. Res. D*
 1142 *Atmos.*, 110(16), 1–11, doi:10.1029/2005JD005866, 2005.

1143 Pan, Y., Tian, S., Zhao, Y., Zhang, L., Zhu, X., Gao, J., Huang, W., Zhou, Y., Song,
1144 Y., Zhang, Q. and Wang, Y.: Identifying Ammonia Hotspots in China Using a National
1145 Observation Network, *Environ. Sci. Technol.*, 52(7), 3926–3934,
1146 doi:10.1021/acs.est.7b05235, 2018.

1147 Parzen, E.: On the Estimation of Probability Density Functions and Mode, *Ann. Math.*
1148 *Stat.*, 33, 1065–1076, 1962.

1149 Paulot, F., Jacob, D. J., Pinder, R. W., Bash, J. O., Travis, K. and Henze, D. K.:
1150 Ammonia emissions in the United States, European Union, and China derived by
1151 high-resolution inversion of ammonium wet deposition data: Interpretation with a new
1152 agricultural emissions inventory (MASAGE-NH3), *J. Geophys. Res. Atmos.*, 119(7),
1153 4343–4364, doi:10.1002/2013JD021130, 2014.

1154 Pinder, R. W., Gilliland, A. B. and Dennis, R. L.: Environmental impact of
1155 atmospheric NH_3 emissions under present and future conditions in the
1156 eastern United States, *Geophys. Res. Lett.*, 35(12), 1–6,
1157 doi:10.1029/2008GL033732, 2008.

1158 Pope III, C. A., Burnett, R. T., Thun, M. J., Calle, E. E., Krewski, D. and Thurston, G.
1159 D.: Lung Cancer, Cardiopulmonary Mortality, and Long-term Exposure to Fine
1160 Particulate Air Pollution, *J. Am. Med. Assoc.*, 287(9), 1132–1141,
1161 doi:10.1001/jama.287.9.1132, 2002.

1162 Quinn, P. K., Bates, T. S. and Johnson, J. E.: Interactions Between the Sulfur and
1163 Reduced Nitrogen Cycles Over the Central Pacific Ocean, *J. Geophys. Res.*,
1164 95(D10), 16405–16416, 1990.

1165 R'Honi, Y., Clarisse, L., Clerbaux, C., Hurtmans, D., Duflo, V., Turquety, S., Ngadi,
1166 Y. and Coheur, P. F.: Exceptional emissions of NH_3 and HCOOH in the 2010
1167 Russian wildfires, *Atmos. Chem. Phys.*, 13(1), 4171–4181, doi:10.5194/acp-13-4171-
1168 2013, 2013.

1169 Reche, C., Viana, M., Pandolfi, M., Alastuey, A., Moreno, T., Amato, F., Ripoll, A. and
1170 Querol, X.: Urban NH_3 levels and sources in a Mediterranean environment, *Atmos.*
1171 *Environ.*, 57, 153–164, doi:10.1016/j.atmosenv.2012.04.021, 2012.

1172 Reis, S., Pinder, R. W., Zhang, M., Lijie, G. and Sutton, M. A.: Reactive nitrogen in
1173 atmospheric emission inventories, *Atmos. Chem. Phys.*, 9(19), 7657–7677,
1174 doi:10.5194/acp-9-7657-2009, 2009.

1175 Renka, R. J.: Multivariate Interpolation of Large Sets of Scattered Data, *ACM Trans.*
1176 *Math. Softw.*, 14(2), 139–148, doi:10.1145/45054.45055, 1988.

1177 Schulz, M.: Constraining model estimates of the aerosol Radiative Forcing,
1178 Université Pierre et Marie Curie, Paris VI., 2007.

1179 Scott, D. W.: Multivariate density estimation: Theory, practice, and visualization:
1180 Second edition., 2015.

1181 Seinfeld, J. H. and Pandis, S. N.: *Atmospheric Chemistry and Physics. From Air*
1182 *Pollution to Climate Change*, 2nd ed., John Wiley & Sons, NY., 2000.

1183 Shephard, M. W. and Cady-Pereira, K. E.: Cross-track Infrared Sounder (CrIS)
1184 satellite observations of tropospheric ammonia, *Atmos. Meas. Tech.*, 8(3), 1323–
1185 1336, doi:10.5194/amt-8-1323-2015, 2015.

1186 Shephard, M. W., McLinden, C. A., Cady-Pereira, K. E., Luo, M., Moussa, S. G.,
1187 Leithead, A., Liggio, J., Staebler, R. M., Akingunola, A., Makar, P., Lehr, P., Zhang,
1188 J., Henze, D. K., Millet, D. B., Bash, J. O., Zhu, L., Wells, K. C., Capps, S. L.,
1189 Chaliyakunnel, S., Gordon, M., Hayden, K., Brook, J. R., Wolde, M. and Li, S. M.:
1190 Tropospheric Emission Spectrometer (TES) satellite observations of ammonia,
1191 methanol, formic acid, and carbon monoxide over the Canadian oil sands: Validation
1192 and model evaluation, *Atmos. Meas. Tech.*, 8(12), 5189–5211, doi:10.5194/amt-8-

1193 5189-2015, 2015.

1194 Shephard, M. W., Dammers, E., E. Cady-Pereira, K., K. Kharol, S., Thompson, J.,
 1195 Gainariu-Matz, Y., Zhang, J., A. McLinden, C., Kovachik, A., Moran, M., Bittman, S.,
 1196 E. Sioris, C., Griffin, D., J. Alvarado, M., Lonsdale, C., Savic-Jovcic, V. and Zheng,
 1197 Q.: Ammonia measurements from space with the Cross-track Infrared Sounder:
 1198 Characteristics and applications, *Atmos. Chem. Phys.*, 20(4), 2277–2302,
 1199 doi:10.5194/acp-20-2277-2020, 2020.

1200 Someya, Y., Imasu, R., Shiomi, K. and Saitoh, N.: Atmospheric ammonia retrieval
 1201 from the TANSO-FTS / GOSAT thermal infrared sounder, , 1990, 309–321, 2020.

1202 Sørensen, L. L., Hertel, O., Skjøth, C. A., Lund, M. and Pedersen, B.: Fluxes of
 1203 ammonia in the coastal marine boundary layer, *Atmos. Environ.*, 37(SUPPL. 1), 167–
 1204 177, doi:10.1016/S1352-2310(03)00247-4, 2003.

1205 Stevens, C. J., Dupr, C., Dorland, E., Gaudnik, C., Gowing, D. J. G., Bleeker, A.,
 1206 Diekmann, M., Alard, D., Bobbink, R., Fowler, D., Corcket, E., Mountford, J. O.,
 1207 Vandvik, V., Aarrestad, P. A., Muller, S. and Dise, N. B.: Nitrogen deposition
 1208 threatens species richness of grasslands across Europe, *Environ. Pollut.*, 158(9),
 1209 2940–2945, doi:10.1016/j.envpol.2010.06.006, 2010.

1210 Streets, D. G., Canty, T., Carmichael, G. R., de Foy, B., Dickerson, R. R., Duncan, B.
 1211 N., Edwards, D. P., Haynes, J. A., Henze, D. K., Houyoux, M. R., Jacob, D. J.,
 1212 Krotkov, N. A., Lamsal, L. N., Liu, Y., Lu, Z., Martin, R. V, Pfister, G. G., Pinder, R.
 1213 W., Salawitch, R. J. and Wecht, K. J.: Emissions estimation from satellite retrievals: A
 1214 review of current capability, *Atmos. Environ.*, 77, 1011–1042,
 1215 doi:https://doi.org/10.1016/j.atmosenv.2013.05.051, 2013.

1216 Sutton, M. A., Fowler, D., Moncrieff, J. B. and Storeton-West, R. L.: The exchange of
 1217 atmospheric ammonia with vegetated surfaces. II: Fertilized vegetation, *Q. J. R.
 1218 Meteorol. Soc.*, 119(513), 1047–1070, doi:10.1002/qj.49711951310, 1993.

1219 Sutton, M. A., Dragosits, U., Tang, Y. S. and Fowler, D.: Ammonia emissions from
 1220 non-agricultural sources in the UK, , 34(August 1999), 2000.

1221 Sutton, M. A., Erisman, J. W., Dentener, F. and Möller, D.: Ammonia in the
 1222 environment: From ancient times to the present, *Environ. Pollut.*, 156(3), 583–604,
 1223 doi:10.1016/j.envpol.2008.03.013, 2008.

1224 Tanvir, A., Khokhar, M. F., Javed, Z., Sandhu, O., Mustansar, T. and Shoaib, A.:
 1225 Spatiotemporal evolution of atmospheric ammonia columns over the indo-gangetic
 1226 plain by exploiting satellite observations, *Adv. Meteorol.*, 2019,
 1227 doi:10.1155/2019/7525479, 2019.

1228 Turner, A. J., Henze, D. K., Martin, R. V. and Hakami, A.: The spatial extent of
 1229 source influences on modeled column concentrations of short-lived species,
 1230 *Geophys. Res. Lett.*, 39(12), 1–5, doi:10.1029/2012GL051832, 2012.

1231 Uematsu, M., Toratani, M., Kajino, M., Narita, Y., Senga, Y. and Kimoto, T.:
 1232 Enhancement of primary productivity in the western North Pacific caused by the
 1233 eruption of the Miyake-jima Volcano, *Geophys. Res. Lett.*, 31(6), n/a-n/a,
 1234 doi:10.1029/2003gl018790, 2004.

1235 Vincenty, T.: Direct and inverse solutions of geodesics on the ellipsoid with
 1236 application of nested equations, *Surv. Rev. XXIII* (misprinted as XXII), 176, 88–93,
 1237 1975.

1238 De Vries, W., Kros, J., Reinds, G. J. and Butterbach-Bahl, K.: Quantifying impacts of
 1239 nitrogen use in European agriculture on global warming potential, *Curr. Opin.
 1240 Environ. Sustain.*, 3(5), 291–302, doi:10.1016/j.cosust.2011.08.009, 2011.

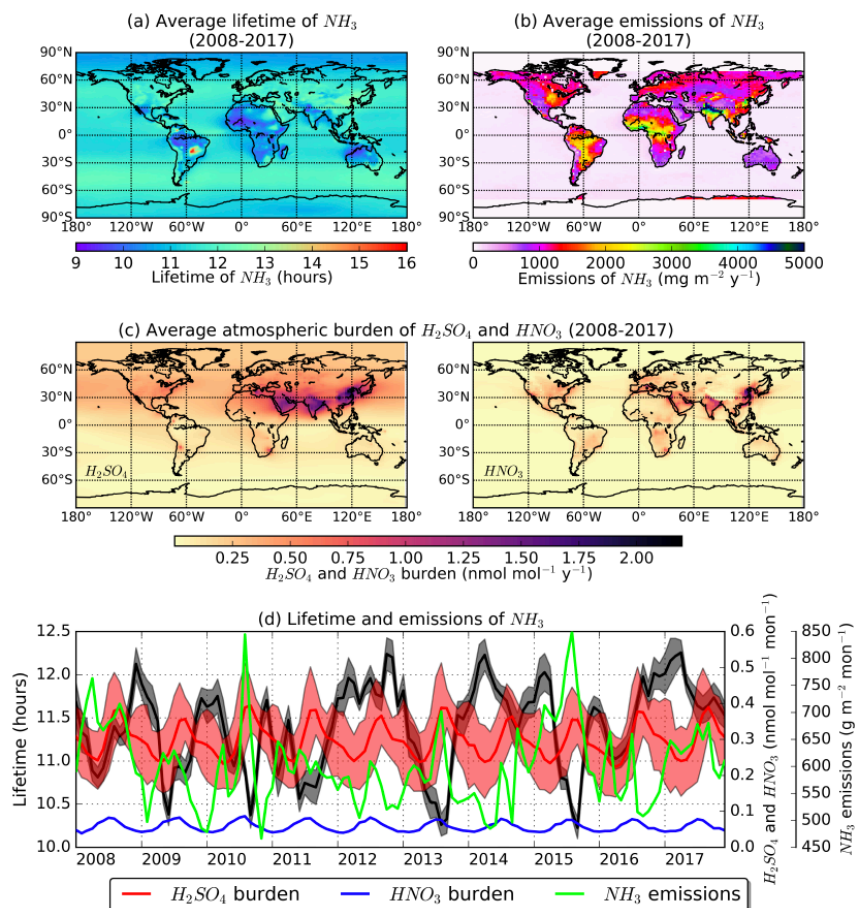
1241 Wang, Y., Zhang, Q. Q., He, K., Zhang, Q. and Chai, L.: Sulfate-nitrate-ammonium
 1242 aerosols over China: Response to 2000-2015 emission changes of sulfur dioxide,

1243 nitrogen oxides, and ammonia, *Atmos. Chem. Phys.*, 13(5), 2635–2652,
1244 doi:10.5194/acp-13-2635-2013, 2013.
1245 Warner, J. X., Dickerson, R. R., Wei, Z., Strow, L. L., Wang, Y. and Liang, Q.:
1246 Increased atmospheric ammonia over the world's major agricultural areas detected
1247 from space, *Geophys. Res. Lett.*, 1–10, doi:10.1002/2016GL072305, 2017.
1248 Webb, J., Menzi, H., Pain, B. F., Misselbrook, T. H., Dämmgen, U., Hendriks, H. and
1249 Döhler, H.: Managing ammonia emissions from livestock production in Europe,
1250 *Environ. Pollut.*, 135(3 SPEC. ISS.), 399–406, doi:10.1016/j.envpol.2004.11.013,
1251 2005.
1252 Whitburn, S., Van Damme, M., Kaiser, J. W., Van Der Werf, G. R., Turquety, S.,
1253 Hurtmans, D., Clarisse, L., Clerbaux, C. and Coheur, P. F.: Ammonia emissions in
1254 tropical biomass burning regions: Comparison between satellite-derived emissions
1255 and bottom-up fire inventories, *Atmos. Environ.*, 121, 42–54,
1256 doi:10.1016/j.atmosenv.2015.03.015, 2014.
1257 Whitburn, S., Van Damme, M., Clarisse, L., Bauduin, S., Heald, C. L., Hadji-Lazaro,
1258 J., Hurtmans, D., Zondlo, M. A., Clerbaux, C. and Coheur, P. F.: A flexible and robust
1259 neural network IASI-NH₃ retrieval algorithm, *J. Geophys. Res.*, 121(11), 6581–6599,
1260 doi:10.1002/2016JD024828, 2016a.
1261 Whitburn, S., Damme, M. Van, Clarisse, L., Turquety, S., Clerbaux, C. and Coheur,
1262 P. -: Peat fires doubled annual ammonia emissions in Indonesia during the 2015 El
1263 Niño, *Geophys. Res. Lett.*, doi:10.1002/2016GL070620, 2016b.
1264 Xu, L. and Penner, J. E.: Global simulations of nitrate and ammonium aerosols and
1265 their radiative effects, *Atmos. Chem. Phys.*, 12(20), 9479–9504, doi:10.5194/acp-12-
1266 9479-2012, 2012.
1267 Xu, P., Liao, Y. J., Lin, Y. H., Zhao, C. X., Yan, C. H., Cao, M. N., Wang, G. S. and
1268 Luan, S. J.: High-resolution inventory of ammonia emissions from agricultural
1269 fertilizer in China from 1978 to 2008, *Atmos. Chem. Phys.*, 16(3), 1207–1218,
1270 doi:10.5194/acp-16-1207-2016, 2016.
1271 Xu, R. T., Pan, S. F., Chen, J., Chen, G. S., Yang, J., Dangal, S. R. S., Shepard, J.
1272 P. and Tian, H. Q.: Half-Century Ammonia Emissions From Agricultural Systems in
1273 Southern Asia: Magnitude, Spatiotemporal Patterns, and Implications for Human
1274 Health, *GeoHealth*, 2(1), 40–53, doi:10.1002/2017gh000098, 2018.
1275 Yang, K., Krotkov, N. A., Krueger, A. J., Carn, S. A., Bhartia, P. K. and Levelt, P. F.:
1276 Retrieval of large volcanic SO₂ columns from the Aura Ozone Monitoring
1277 Instrument: Comparison and limitations, *J. Geophys. Res. Atmos.*, 112(24), 1–14,
1278 doi:10.1029/2007JD008825, 2007.
1279 Zavyalov, V., Esplin, M., Scott, D., Esplin, B., Bingham, G., Hoffman, E., Lietzke, C.,
1280 Predina, J., Frain, R., Suwinski, L., Han, Y., Major, C., Graham, B. and Phillips, L.:
1281 Noise performance of the CrIS instrument, , 118, 108–120,
1282 doi:10.1002/2013JD020457, 2013.
1283 Zhao, C. and Wang, Y.: Assimilated inversion of NO_x emissions over east Asia using
1284 OMINO₂ column measurements, *Geophys. Res. Lett.*, 36(6), 1–5,
1285 doi:10.1029/2008GL037123, 2009.
1286 Zhu, L., Henze, D. K., Cady-Pereira, K. E., Shephard, M. W., Luo, M., Pinder, R. W.,
1287 Bash, J. O. and Jeong, G. R.: Constraining U.S. ammonia emissions using TES
1288 remote sensing observations and the GEOS-Chem adjoint model, *J. Geophys. Res.*
1289 *Atmos.*, 118(8), 3355–3368, doi:10.1002/jgrd.50166, 2013.
1290 Zhu, L., Henze, D. K., Bash, J. O., Cady-Pereira, K. E., Shephard, M. W., Luo, M.
1291 and Capps, S. L.: Sources and Impacts of Atmospheric NH₃: Current Understanding
1292 and Frontiers for Modeling, Measurements, and Remote Sensing in North America,

1293 Curr. Pollut. Reports, 1(2), 95–116, doi:10.1007/s40726-015-0010-4, 2015.
1294
1295

1296 FIGURE LEGENDS

1297



1298

1299 Figure 1. (a) 10-year average model lifetime of ammonia calculated from the LMDz-OR-INCA,

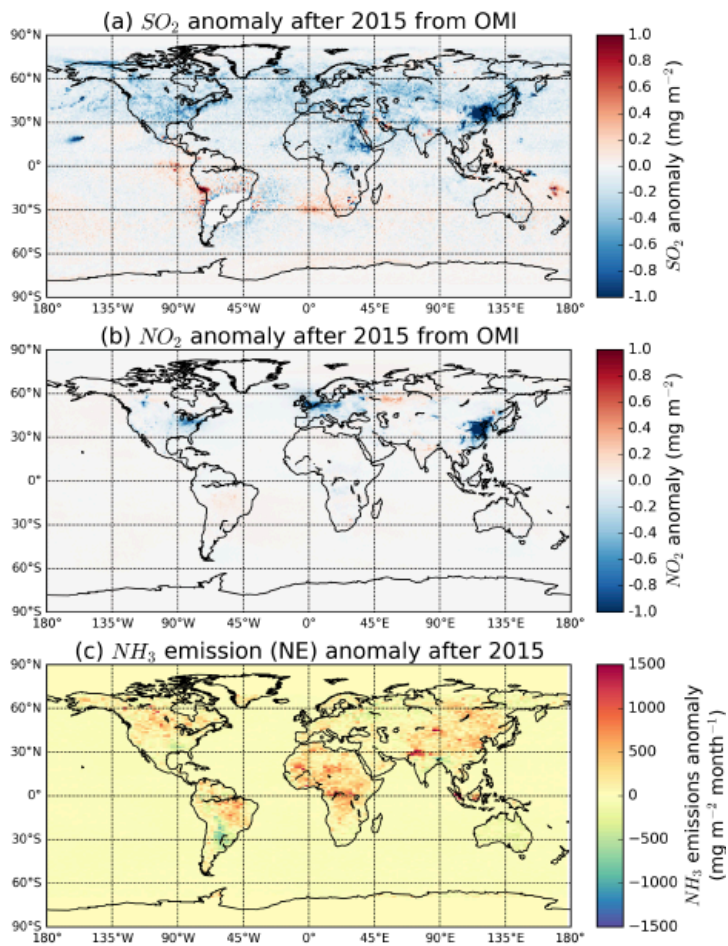
1300 (b) total annual emissions averaged over the 10-year period (NE emissions), (c) atmospheric

1301 burden of the reactants sulfuric and nitric acid calculated in the model, and (d) monthly

1302 timeseries of lifetime (black), ammonia emissions (green), sulfuric (red) and nitric acid column

1303 concentrations (blue) for the whole 10-year period.

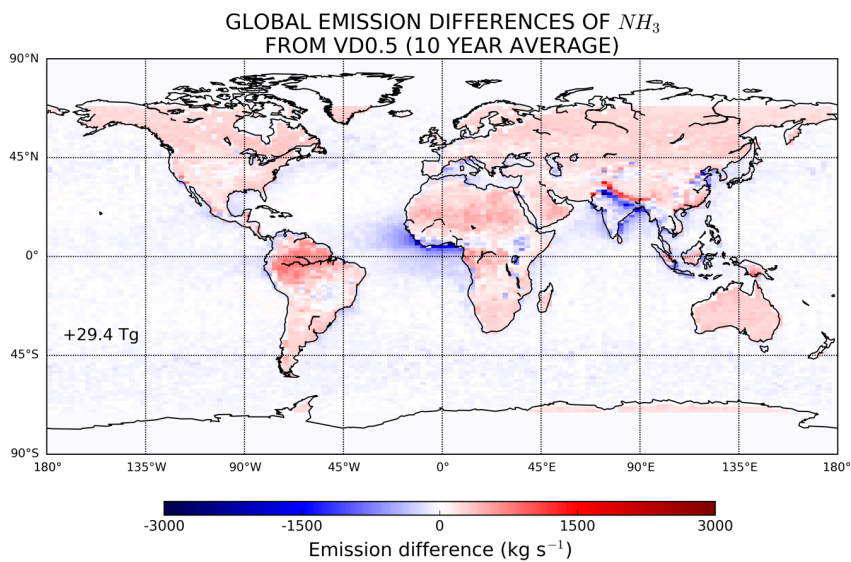
1304



1305

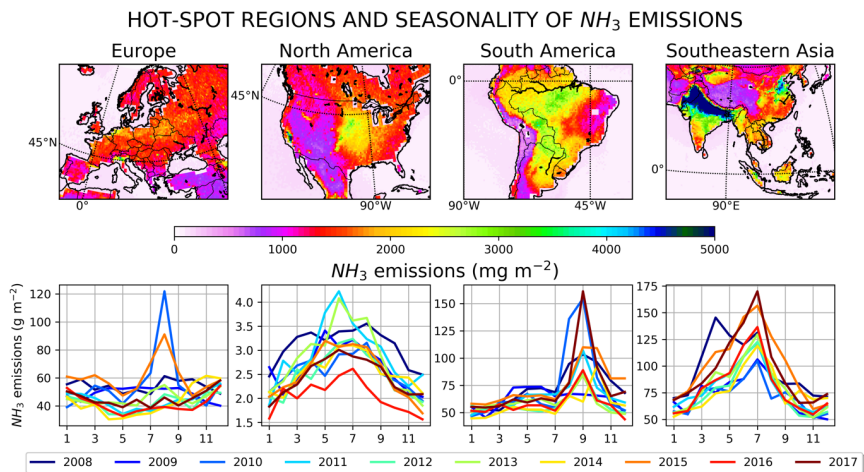
1306 Figure 2. Annual average total column (a) sulfur dioxide and (b) nitrogen dioxide anomaly
 1307 after 2015 from OMI, and (c) annual average emission anomaly of ammonia calculated from
 1308 IASI in the present study (NE).

1309



1310
 1311 Figure 3. Global differences of ammonia emissions calculated in the present study (NE) from
 1312 those calculated using Van Damme et al. (2018) gridded concentrations applying a constant
 1313 lifetime of 0.5 days (VD0.5). The results are given as 10-year average (2008–2017) and the
 1314 number denotes the annual difference in the emissions.

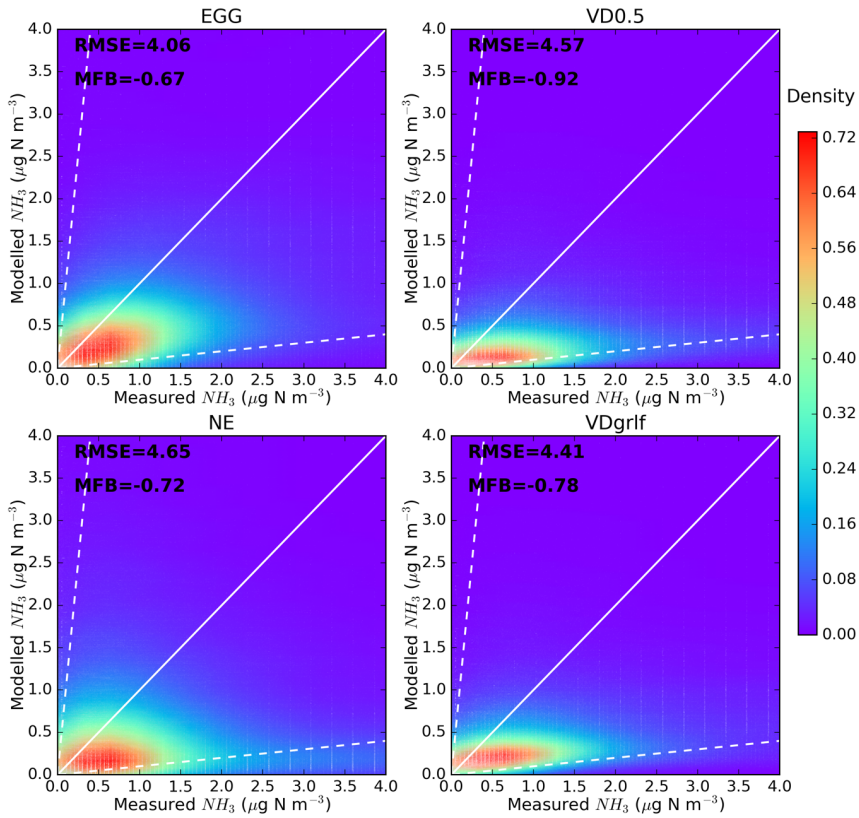
1315



1316
 1317 Figure 4. Total annual emissions of ammonia averaged over the 10-year period (2008–2017) in
 1318 Europe, North and South America and Southeastern Asia, which are regions characterized by
 1319 the largest contribution to global ammonia budget. In the bottom panels the monthly variation
 1320 of the emissions is shown for each year of the study period.

1321

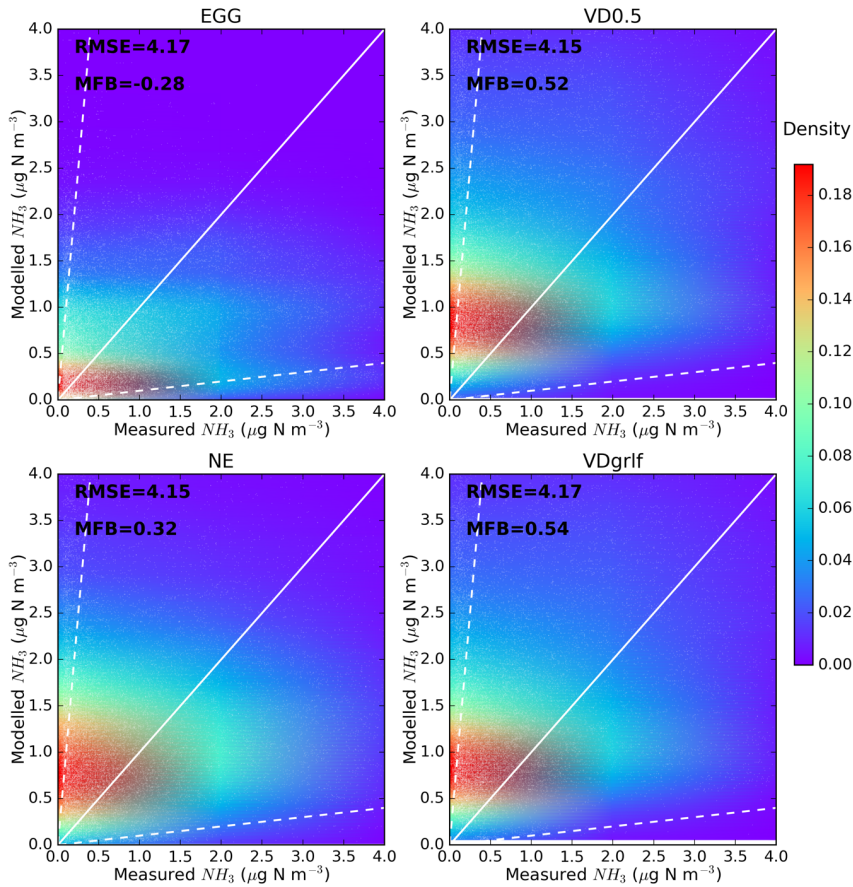
**COMPARISON WITH OBSERVATIONS FROM EMEP
(N=299075)**



1322
1323 Figure 5. Validation of modelled concentrations of ammonia for different emissions datasets
1324 (EGG, VD0.5, NE and VDgrif) against ground-based measurements from EMEP for the 10-
1325 year (2008–2017) study period. Scatterplots of modelled against measured concentrations for
1326 the aforementioned emission inventories were plotted with the Kernel density estimation, which
1327 is a way to estimate the probability density function (PDF) of a random variable in a non-
1328 parametric way.

1329

**COMPARISON WITH OBSERVATIONS FROM AMON
(N=27096)**

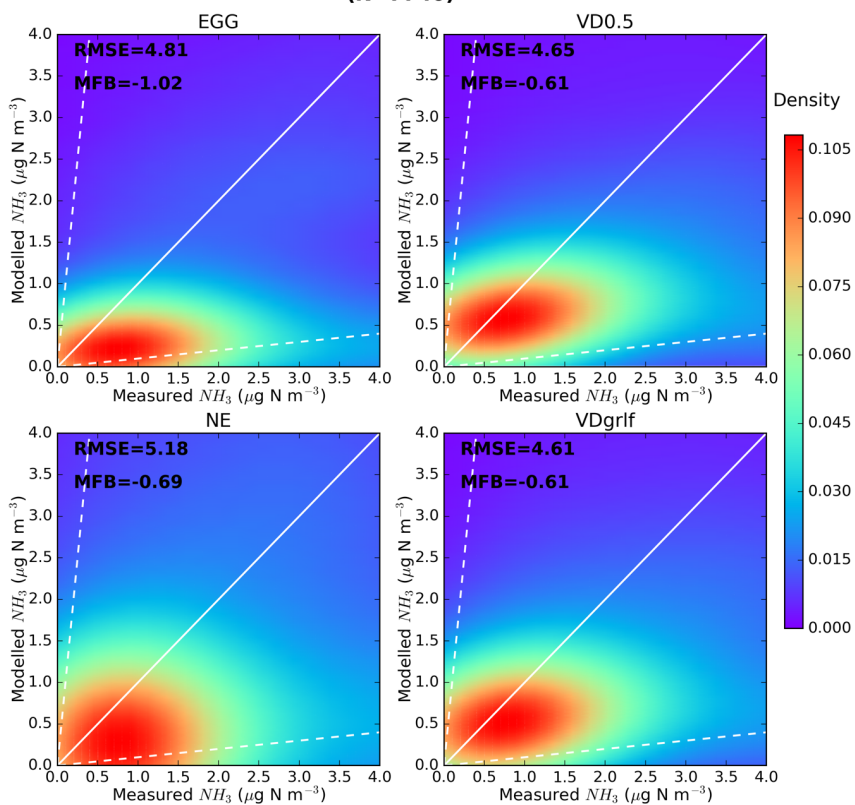


1330

1331 Figure 6. Validation of modelled concentrations of ammonia for different emissions datasets
1332 (EGG, VD0.5, NE and VDgrif) against ground-based measurements from AMON for the 10-
1333 year (2008–2017) study period. Scatterplots of modelled against measured concentrations for
1334 the aforementioned emission inventories were plotted with the Kernel density estimation, which
1335 is a way to estimate the probability density function (PDF) of a random variable in a non-
1336 parametric way.

1337

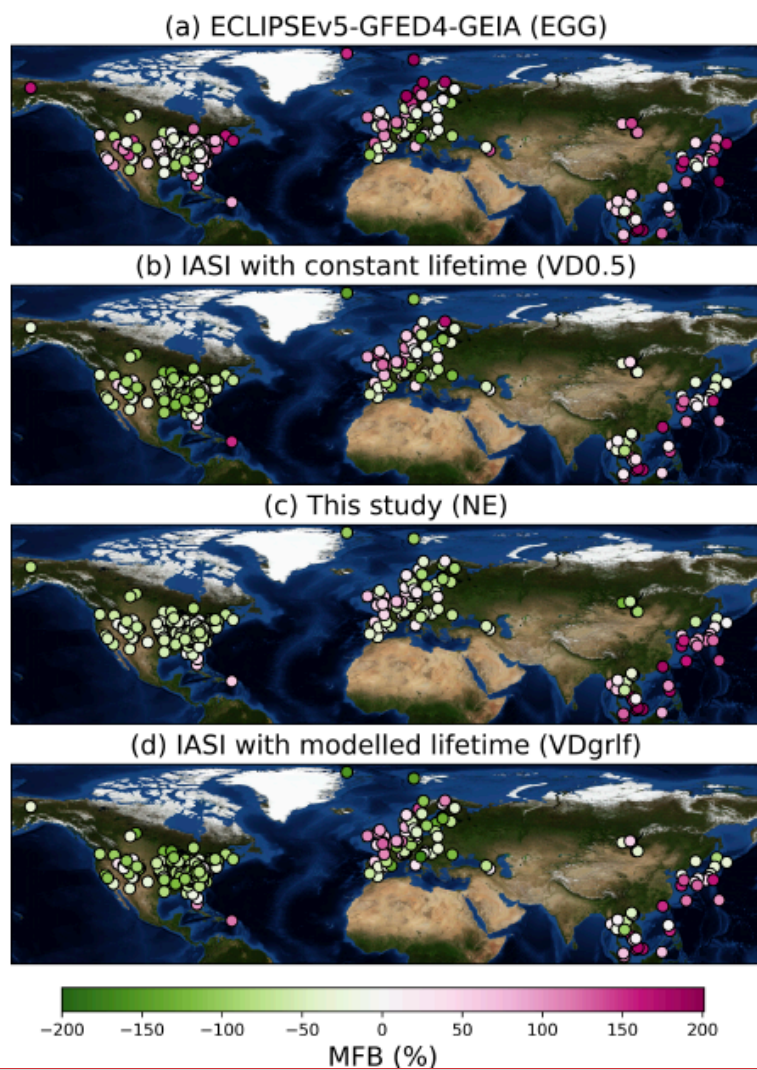
**COMPARISON WITH OBSERVATIONS FROM EANET
(N=7740)**



1338

1339 Figure 7. Validation of modelled concentrations of ammonia for different emissions datasets
 1340 (EGG, VD0.5, NE and VDgrlf) against ground-based measurements from EANET for the 10-
 1341 year (2008–2017) study period. Scatterplots of modelled against measured concentrations for
 1342 the aforementioned emission inventories were plotted with the Kernel density estimation, which
 1343 is a way to estimate the probability density function (PDF) of a random variable in a non-
 1344 parametric way.

1345



1346

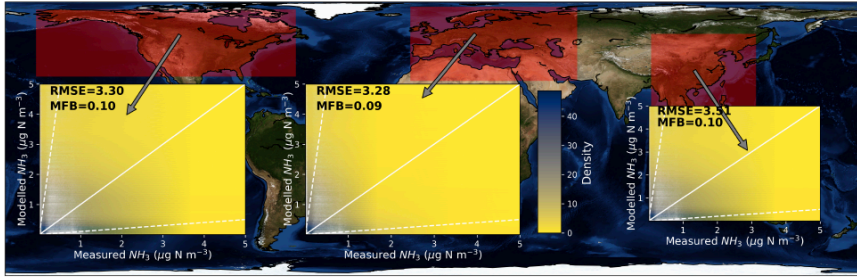
1347 **Figure 8. Overview of the comparison with ground-based measurements of ammonia. MFB**
 1348 **for each of the stations from AMoN, EMEP and EANET monitoring stations calculated after**
 1349 **running LMDz-OR-INCA with the emissions of EGG, VD0.5, NE and VDgrlf for the period**
 1350 **2008–2017.**

1351

Formatted: Font: (Default) Times New Roman, 12 pt, Not Bold, Font colour: Text 1, Shadow

Formatted: Left

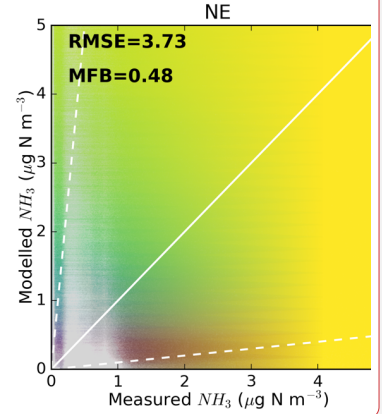
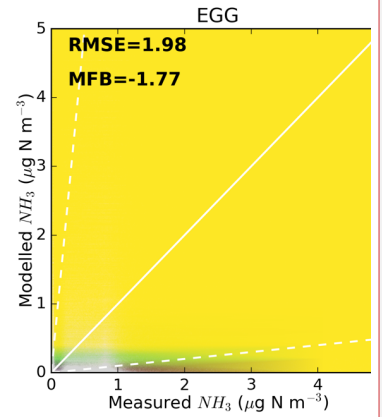
COMPARISON WITH OBSERVATIONS FROM CRIS



1352 Figure 9. Kernel density estimation (KDE) of the probability density function (PDF) of
 1353 modelled versus CrIS concentrations of ammonia in a non-parametric way. Modelled
 1354 concentrations are results of simulations using NE emissions datasets for the period 2012–2017,
 1355 for which CrIS data were available. The comparison is shown for North America, Europe and
 1356 Southeastern Asia.
 1357

1358

COMPARISON WITH CRIS (N=)

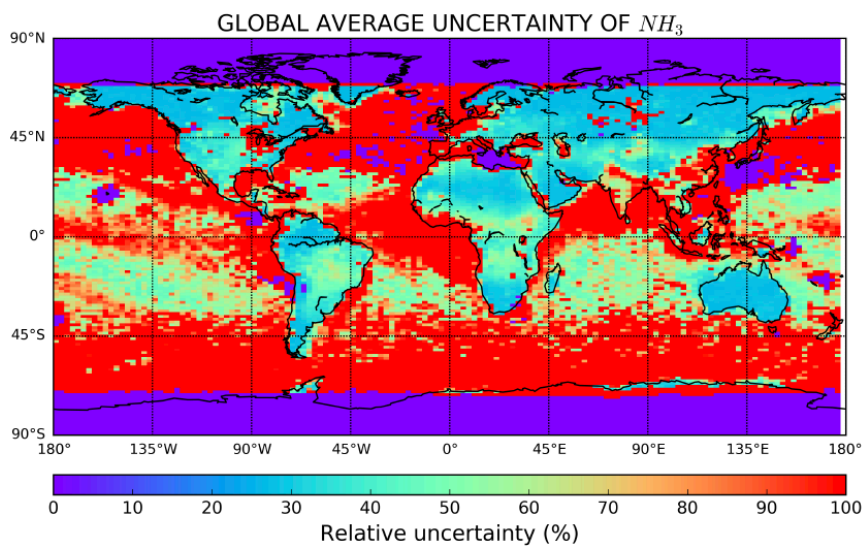


Deleted:

Deleted: 8

Deleted: different

Deleted: (EGG, VD0.5, NE and VDgrlf)



1363
 1364 Figure 10, 10-year average relative uncertainty of modelled surface concentrations expressed
 1365 as the standard deviation of surface concentrations from a model ensemble (Table 1) divided
 1366 by the average.

Deleted: 9
 Deleted: Table 1

1367

1370 Table 1. Model ensemble simulations using different emissions for ammonia that were used in
 1371 the calculations of uncertainty. Uncertainties were calculated as the standard deviation of the
 1372 surface concentrations of ammonia from the 10 ensemble members for the 10-year period
 1373 (2008–2017).

	Parameter perturbed	10-year average emissions (Tg yr ⁻¹)
Ensemble 1	$d_k = 0$ in Eq. 2	121±50.6
Ensemble 2	$d_k = 10$ in Eq. 2	175±33.3
Ensemble 3	$d_k = 20$ in Eq. 2	189±28.7
Ensemble 4	$d_k = 60$ in Eq. 2	218±15.5
Ensemble 5	$d_k = 100$ in Eq. 2	208±51.8
Ensemble 6	$d_k = 500$ in Eq. 2	223±26.5
Ensemble 7	EGG	65±2.8
Ensemble 8	VD0.5	189
Ensemble 9	NE	213±18.1
Ensemble 10	VDgrlf	201±10.4

1374

1375

1376 **SUPPLEMENTARY FIGURE LEGENDS**

1377

1378 **Figure S 1.**

1379

1380 **Figure S 2.**

1381

1382 **Figure S 3.**

1383

1384 **Figure S 4.**

1385

1386 **Figure S 5.**

1387

1388 **Figure S 6.**

1389

1390 **Figure S 7.**

1391

1392 **Figure S 8.**

1393

1394 **Figure S 9.**

1395

1396 **Figure S 10.**

1397

1398 **Figure S 11.**